AN RAI OF DATA
GENERALIZING THE DATA-DRIVEN ROCKFALL ACTIVITY INDEX (RAI) BASED ON LONG-TERM OBSERVATIONS OF WELL-CHARACTERIZED SLOPES

FINAL PROJECT REPORT

by

Margaret M. Darrow
Daisy M. Herrman
University of Alaska Fairbanks

Ben Leshchinsky
Michael J. Olsen
Oregon State University

Joseph Wartman
University of Washington

Sponsorship
University of Alaska Fairbanks, Oregon State University,
University of Washington for

Pacific Northwest Transportation Consortium (PacTrans) USDOT University Transportation
Center for Federal Region 10 University of Washington
More Hall 112, Box 352700
Seattle, WA 98195-2700

In cooperation with U.S. Department of Transportation,
Office of the Assistant Secretary for Research and Technology (OST-R)

DISCLAIMER

TECHNICAL REPORT DOCUMENTATION PAGE

1. Report No.	**2. Government Accession No.** 01872466	**3. Recipient's Catalog No.**

4. Title and Subtitle AN RAI OF DATA: GENERALIZING THE DATA-DRIVEN ROCKFALL ACTIVITY INDEX (RAI) BASED ON LONG-TERM OBSERVATIONS OF WELL-CHARACTERIZED SLOPES	**5. Report Date** 4/18/2023 **6. Performing Organization Code**
7. Author(s) and Affiliations Margaret M. Darrow, 0000-0003-4078-4746; Daisy M. Herrman; University of Alaska Fairbanks Ben Leshchinsky, 0000-0003-3890-1368; Oregon State University; Michael J. Olsen, 0000-0002-2989-5309; Oregon State University	**8. Performing Organization Report No.** 2022-M-UAF-2
9. Performing Organization Name and Address PacTrans Pacific Northwest Transportation Consortium University Transportation Center for Federal Region 10 University of Washington More Hall 112 Seattle, WA 98195-2700	**10. Work Unit No. (TRAIS)** **11. Contract or Grant No.** 69A3551747110
12. Sponsoring Organization Name and Address United States Department of Transportation Research and Innovative Technology Administration 1200 New Jersey Avenue, SE Washington, DC 20590	**13. Type of Report and Period Covered** Research, 1/16/2022-4/15/2023 **14. Sponsoring Agency Code**

15. Supplementary Notes

Report uploaded to: www.pactrans.org

16. Abstract

In previous PacTrans research, the research team developed the Rockfall Activity Index system (RAI), a point cloud-derived, high-resolution, morphology-based approach for identifying, assessing, and mapping rockfall hazards at a high resolution across the entire surface of a rock slope. Continued monitoring at sites in both Alaska and Oregon has shown that rockfall activity is variable as a function of geology and rock properties. In this research, we used geologic characterization, analysis of change from light detection and ranging (lidar) differencing, and collection of 4,800 Schmidt Hammer measurements to constrain relationships between geologic structure and rockfall activity at a variety of rock slopes. Generally, lower Schmidt hammer rebound measurements were observed in areas with higher activity rates, suggesting that rebound (especially when corrected per ASTM standards) may be an effective proxy for rockfall activity or susceptibility. However, the large variability in these measurements, particularly between sites, suggests that these measurements are best applied on a site-specific basis. Additionally, we computed rockfall volumes to analyze mobility impacts by using an empirical relationship derived from the Rockfall Impacts to Mobility (RIM) database, demonstrating the importance of linking rockfall activity and hazard. Future work could look at expanding databases of rockfall impacts to mobility, collect more Schmidt hammer measurements, collect more epochs of rock slope digital terrain models, and further connect rock slope weathering and structure to the RAI analysis.

17. Key Words Rockfalls, laser radar, engineering geology, Schmidt hammer, strength testing	**18. Distribution Statement**

19. Security Classification (of this report) Unclassified.	**20. Security Classification (of this page)** Unclassified.	**21. No. of Pages** 37	**22. Price** N/A

Form DOT F 1700.7 (8-72) **Reproduction of completed page authorized.**

SI* (MODERN METRIC) CONVERSION FACTORS

APPROXIMATE CONVERSIONS TO SI UNITS				
Symbol	**When You Know**	**Multiply By**	**To Find**	**Symbol**
		LENGTH		
in	inches	25.4	millimeters	mm
ft	feet	0.305	meters	m
yd	yards	0.914	meters	m
mi	miles	1.61	kilometers	km
		AREA		
in^2	square inches	645.2	square millimeters	mm^2
ft^2	square feet	0.093	square meters	m^2
yd^2	square yard	0.836	square meters	m^2
ac	acres	0.405	hectares	ha
mi^2	square miles	2.59	square kilometers	km^2
		VOLUME		
fl oz	fluid ounces	29.57	milliliters	mL
gal	gallons	3.785	liters	L
ft^3	cubic feet	0.028	cubic meters	m^3
yd^3	cubic yards	0.765	cubic meters	m^3
		NOTE: volumes greater than 1000 L shall be shown in m^3		
		MASS		
oz	ounces	28.35	grams	g
lb	pounds	0.454	kilograms	kg
T	short tons (2000 lb)	0.907	megagrams (or "metric ton")	Mg (or "t")
		TEMPERATURE (exact degrees)		
°F	Fahrenheit	5 (F-32)/9 or (F-32)/1.8	Celsius	°C
		ILLUMINATION		
fc	foot-candles	10.76	lux	lx
fl	foot-Lamberts	3.426	candela/m^2	cd/m^2
		FORCE and PRESSURE or STRESS		
lbf	poundforce	4.45	newtons	N
lbf/in^2	poundforce per square inch	6.89	kilopascals	kPa

APPROXIMATE CONVERSIONS FROM SI UNITS				
Symbol	**When You Know**	**Multiply By**	**To Find**	**Symbol**
		LENGTH		
mm	millimeters	0.039	inches	in
m	meters	3.28	feet	ft
m	meters	1.09	yards	yd
km	kilometers	0.621	miles	mi
		AREA		
mm^2	square millimeters	0.0016	square inches	in^2
m^2	square meters	10.764	square feet	ft^2
m^2	square meters	1.195	square yards	yd^2
ha	hectares	2.47	acres	ac
km^2	square kilometers	0.386	square miles	mi^2
		VOLUME		
mL	milliliters	0.034	fluid ounces	fl oz
L	liters	0.264	gallons	gal
m^3	cubic meters	35.314	cubic feet	ft^3
m^3	cubic meters	1.307	cubic yards	yd^3
		MASS		
g	grams	0.035	ounces	oz
kg	kilograms	2.202	pounds	lb
Mg (or "t")	megagrams (or "metric ton")	1.103	short tons (2000 lb)	T
		TEMPERATURE (exact degrees)		
°C	Celsius	1.8C+32	Fahrenheit	°F
		ILLUMINATION		
lx	lux	0.0929	foot-candles	fc
cd/m^2	candela/m^2	0.2919	foot-Lamberts	fl
		FORCE and PRESSURE or STRESS		
N	newtons	0.225	poundforce	lbf
kPa	kilopascals	0.145	poundforce per square inch	lbf/in^2

*SI is the symbol for the International System of Units. Appropriate rounding should be made to comply with Section 4 of ASTM E380.
(Revised March 2003)

TABLE OF CONTENTS

LIST OF FIGURES

LIST OF TABLES

LIST OF ABBREVIATIONS

ADOT&PF:	Alaska Department of Transportation and Public Facilities
ASTM:	American Society for Testing and Materials
CV:	Canyonville
EV:	Eddyville
f:	median time-normalized failure rate
f_i:	inter-epochal failure rates
GPS:	Global Positioning System
Lidar:	Light detection and ranging
LL71:	Long Lake MP71
MP:	Milepost
NC241:	Nenana Canyon MP241
ODOT:	Oregon Department of Transportation
PacTrans:	Pacific Northwest Transportation Consortium
PNW:	Pacific Northwest
r:	activity rate
R:	Schmidt hammer rebound value
RAI:	Rockfall Activity Index
RIM:	Rockfall Impacts to Mobility
SH:	Schmidt hammer
SR:	State route
UAS:	Unmanned aircraft systems
WSDOT:	Washington State Department of Transportation

ACKNOWLEDGMENTS

This work could not have happened without the gracious cooperation of personnel from the Alaska Department of Transportation and Public Facilities, the Washington State Department of Transportation, and the Oregon Department of Transportation. The authors thank Leica Geosystems for providing software and equipment used in this research. Peyton Pressler, Bipin Peethambaran, and Bryce Berrett from OSU assisted with the field data collection associated with this project. Peyton Pressler also assisted with data processing.

EXECUTIVE SUMMARY

With the support of previous PacTrans funding, members of our research team developed the Rockfall Activity Index system (RAI), a point cloud-derived, high-resolution, morphology-based approach for identifying, assessing, and mapping rockfall hazards at a high resolution across the entire surface of the slope. Ongoing assessment of the RAI has indicated that the activity rates are not always consistent, generic values, but instead vary as a function of geology and rock material properties. In this project, we continued from and expanded on years of previous PacTrans research by 1) collecting another epoch of terrestrial laser scanning data from six Alaskan sites and four sites in Washington and Oregon, all with extensive rock slopes adjacent to major highways; 2) characterizing the geology and major discontinuities of the Washington and Oregon sites; and 3) collecting 4,800 Schmidt hammer measurements from the field sites for a systematic evaluation of this tool to determine rock strength and to compare rebound values to rockfall activity rates. Coupled with site characterizations for the Alaska field sites presented by Darrow et al. (2022), the descriptions and discontinuity measurements presented here for the Washington and Oregon sites provide a framework for future studies of these rock slopes, such as kinematic or overall slope stability analyses.

A companion PacTrans-funded project report provides more detail on the Schmidt hammer testing (Herrman and Darrow, in review); however, a systematic comparison of Schmidt hammer measurements to rockfall activity rates demonstrated a modest negative correlation using a power-law relationship. Specifically, there was a tendency to have lower Schmidt hammer rebound values in areas where we observed higher rockfall activity rates. There was, however, significant variability in these results, and we suggest that such analyses should be evaluated on a site-by-site basis. Evaluation of uncorrected and corrected (per ASTM standards) Schmidt hammer rebound values demonstrated that the correction procedure provides a modest improvement of the correlation with rockfall activity.

Further research could explore whether other correction procedures provide better, more representative fits, including that associated with user bias.

Activity rates at each site varied significantly by year, but median and average values demonstrated reasonable correlation with Schmidt hammer rebound values. We suggest that prolonged monitoring and light detection and ranging (lidar) differencing, as well as repeated collection of Schmidt hammer measurements, may lead to reduced uncertainty and more robust

correlations, potentially at scales more generalizable to other rock slopes. Evaluation of more geologic units with diverse structural controls may demonstrate the utility (or lack thereof) of Schmidt hammer measurements as a proxy for rockfall activity rates. Furthermore, we recommend using activity values suggested by Markus (2018) as the baseline parameters for RAI analysis.

We computed rockfall volumes to perform an analysis of mobility impacts using an empirical relationship derived from the Rockfall Impacts to Mobility (RIM) database. While the approaches that we used accurately quantified that material had fallen from the rock slope, the amount of material that entered the roadway and had direct mobility impacts was not well understood. Additionally, we did not investigate the impact on maintenance activities to clean debris from the catch ditches. Ultimately, a scale factor would help to calibrate the application of the RIM model to produce more realistic closure time values based on material that requires immediate cleanup. Because the RIM model was developed on the basis of larger episodic events, an additional model based on smaller, more frequent events would be useful to quantify shorter but more frequent delays to motorists. Additionally, the long-term effectiveness of rock slope modification techniques and the associated impacts on mobility have not been quantified. While this research and previous PacTrans research indicated a reduction in RAI scores by reducing the amount of overhang, the long-term evolution of rock slopes requires further investigation. Future research can evaluate the impacts of these modifications to reduce material entering the highway.

CHAPTER 1. PROJECT MOTIVATION AND BACKGROUND

1.1. Introduction

Slopes pose a significant hazard to transportation infrastructure and mobility across the Pacific Northwest (PNW) because of the combination of the region's geology, topographic relief, high precipitation rates, and elevated seismicity. Rockfall hazards result in frequent road closures, lane restrictions, infrastructure damage, loss of life, and injuries to motorists, cyclists, and pedestrians. Thus, rockfall directly impacts driver safety, mobility, and accessibility for many critical lifelines. Recent PacTrans-supported research by Holtan (2021) documented the significant mobility and economic impacts that rockfall has on major roads across the PNW, including road closures for a month or more and emergency repair costs of over $1 million for large events.

With the support of PacTrans, our team developed the Rockfall Activity Index system (RAI), a point cloud-derived, high-resolution, morphology-based approach for identifying, assessing, and mapping rockfall hazards at a high resolution across the entire surface of the slope (Dunham et al. 2017). The ultimate purpose of this new research is to improve and refine both the accuracy and interpretation of the RAI analysis to promote its wider adoption by transportation authorities and consulting engineers in the PNW and across the nation.

With the RAI methodology, rockfall hazards are evaluated in a two-step process. First, morphological indices (local slope and roughness) are used to classify mass wasting processes acting on a rock slope. These classifications then are used with estimated instability rates to map rockfall activity across an entire slope face. Developed with roadway safety and impacts in mind, the RAI quantifies rockfall hazard as a function of the annual kinetic energy produced by rockfall along 1-m-long segments. The RAI has been applied in Alaska, Oregon, and New Zealand, among other locations in the U.S. and abroad. A key benefit of RAI analysis is that results are easy to visualize and understand, thereby enabling transportation agencies and consulting engineers to communicate hazards to decision-makers effectively and to identify highly focused mitigation strategies. Recently, the RAI has been implemented in a user-friendly software called *RAMBO* (Olsen et al. 2020) for ease of adoption by practitioners.

In recent research, the team assessed the efficacy, accuracy, and reliability of the RAI methodology and concluded that the automated morphological mapping is highly reliable but that the activity rates for the morphological classes vary more widely than initially estimated by

Dunham et al. (2017). These activity rates, which quantify the “activity "or instability rate of the morphological classes, directly control the RAI mapping of rockfall “hotspots.” Our verification and accuracy studies of the RAI suggested that the activity rates are not always consistent, generic values but instead vary as a function of geology and rock material properties (e.g., well-indurated, freshly weathered crystalline rocks are less active than softer fine-grained rocks, such as siltstones) and local climate conditions (e.g., precipitation rates, number of freeze-thaw cycles, wind loading).

On the basis of numerous discussions and consultations with practitioners, we believe that improving the accuracy of hotspot mapping will lead to more widespread adoption of the RAI by practitioners in the PNW and other parts of the country. Accordingly, in this project, we characterized rock slopes for which we had previously conducted RAI analysis. We compared the estimated RAI activity rate to Schmidt hammer measurements made at thoroughly characterized test sites across a range of geologic and climate settings in Alaska, Washington, and Oregon. The Schmidt hammer is a well-established, widely adopted (Aydin and Basu 2005; Wang and Wan 2019), and easy-to-use field instrument for assessing rock strength in the field (it is also used in practice for estimating the in-place stiffness of the strength of concrete). The team previously developed high-resolution, multi-year change detection data for each site, which are among the best-documented rock slopes in the United States. As the models developed to evaluate rockfall hazard require multiple collections of light detection and ranging (lidar) data for change assessment, we selected sites with previous epochs of data. This enabled evaluation of uncertainty in rockfall rates, as well as of more representative long-term rockfall activity. Furthermore, we refined the qualitative and quantitative information about the geologic conditions of these sites, enabling further refinement of the RAI analysis.

1.2. Research Background

The RAI (Dunham et al. 2017) is computed for each 1-m-long segment of rock slope as:

$$\sum_{i=1}^{n} \frac{1}{2} m_i v_i^2 r_j$$

Eqn 1

where ½ mv^2 represents the kinetic energy of falling rock, n is the number of rock slope cells within a 1-m segment, i is the cell number, r is the instability rate for each morphology classification, and j is the number of morphology classifications within a 1-m segment. Mass is determined as the product of rock volume and specific gravity. The estimated volume is based on the cell area multiplied by an assumed failure depth (Dunham et al., 2017). Velocity computations are based upon a select free fall distance between the point of release and the toe of the rock slope (for transportation corridors, the latter typically corresponds to the road surface elevation). The "activity" rate (r) is the fraction of cells within a morphologic unit that is expected to fail over a typical one-year period. We initially estimated r based on change detection from a single year of observations at a limited number of study sites in Alaska. As high-resolution change detection data are not available for most common projects, we provided estimates of what we believed to be realistic ranges of r for each morphological category. Our recent validation assessment indicated that while the automated morphological mapping is highly reliable, r varies more widely than initially estimated. Indeed, as originally recognized by Dunham et al. (2017), "it should be recognized that r represents rock slope activity rates, which vary based on rock type, weathering, subsurface characteristics (e.g., discontinuity orientation, groundwater level), and environmental conditions, among other factors…it should be understood that these values are associated with a high degree of variability and uncertainty."

The Rockfall Impacts to Mobility (RIM) database was another product created in a previous PacTrans research project by web crawling for rockfall events in media articles, and its primary purpose is to be a database that tracks the relationship between closure time and volume without being constrained to state lines (Holtan 2021). Despite the variability in reported data in media articles, we created a consistent workflow to extract relevant volume and closure data from each catalogued event. Overall, the database we created has 98 entries from which an empirical relationship between rockfall volumes and closure times was derived:

$$\text{ClosureTime} = 0.393*\text{Volume}^{0.756} \qquad \text{Eqn. 2}$$

where ClosureTime is in hours and Volume is in cubic yards. This relationship can be incorporated into the RAI methodology such that anticipated annual closure times can be estimated for highway corridors. This is because the activity rates from the RAI can be multiplied by the source area and estimated failure depths to compute volumes.

1.3. Research Approach and Report Structure

This project consisted of the following tasks. The report chapters that address results of the tasks are indicated in italics and parentheses.

- **Task 1** ***(CHAPTER 2):*** Collect additional sets of terrestrial laser scanning data and potentially unmanned aircraft systems (UAS) structure from motion/multi-view stereo photogrammetry data for slopes in Alaska, Washington, and Oregon.
- **Task 2** ***(CHAPTER 2):*** Conduct a site characterization of each Washington and Oregon field site to map local bedrock geology and determine rock strength through field tests for all field sites.
- **Task 3** ***(CHAPTER 3):*** Analyze the time-series of rockfall rates (m^3/m^2/year) for selected Alaska and Oregon rock slopes (sites with extensive and relatively fewer lidar data collections, respectively).
- **Task 4** ***(CHAPTER 3):*** Develop a practice-oriented activity rate selection methodology.
- **Task 5** ***(CHAPTER 3):*** Perform mobility analysis based on activity rates.
- **Task 6** ***(CHAPTER 4):*** Integrate and summarize findings in reports and outreach activities.

CHAPTER 2. SITE CHARACTERIZATIONS

2.1. Methods

We collected field data during two campaigns: June 8-12, 2022, for the Alaska sites; August 15-19, 2022, for the Oregon sites (see Figure 2.1 for locations); and February 11, 2022, and August 15, 2022, for the southern Washington site. We collected terrestrial lidar data in Alaska using a Maptek LR3 with a pair of Leica GS18s for georeferencing (base and rover). At the Oregon and Washington sites, we used a Leica P50 laser scanner with a combination of Leica GS18s and GS14s for data collection. In addition, the Oregon sites had been previously scanned for an Oregon Department of Transportation (ODOT) research project (Olsen et al. 2020), which provided baseline data for this project. The field campaigns and processing methods were similar to those outlined in Olsen et al. (2020). At the Washington Hewett Lake, Oregon Yellow Creek, and Oregon Eddyville sites, targets were placed over control points and other locations in the scene to help improve the relative accuracy among scans for improved change detection.

At any given site, two or more individuals collected the lidar data, while the other team members mapped bedrock structural features and obtained Schmidt hammer measurements. For the Alaska sites, we also collected representative rocks from each location for unconfined compressive strength testing as part of a related PacTrans-funded project (Herrman and Darrow, in review). For the Washington and Oregon sites, we used “Geopads” to conduct the geologic mapping (please refer to Darrow et al. (2022) for descriptions of the Alaskan site characterizations). Geopads are iPad minis (5th generation) in rugged, waterproof cases that incorporate a BadElf GPS unit for determining position.

We used the FieldMove software to measure the orientations of bedding, joints, and faults. Once back in the office, we used Rocscience Dips to analyze the structural data.

At all sites we collected readings using two, calibrated Schmidt hammer (SH) devices (Rock Schmidt Rebound Hammer Type N with impact energy 2.207 Nm (1.63ft-lbf) and Rock Schmidt Test Hammer, Type L with impact energy 0.735 Nm (0.54ft-lbf)) to conduct a systematic comparison for multiple rock types and weathering conditions in a field setting (Figure 2.2). Two individuals conducted the testing with both hammer types. All SH tests were conducted following American Society for Testing and Materials (ASTM) standards (ASTM 2014) with the exception that we did not use the grinding stone on the *in situ* rock surface.

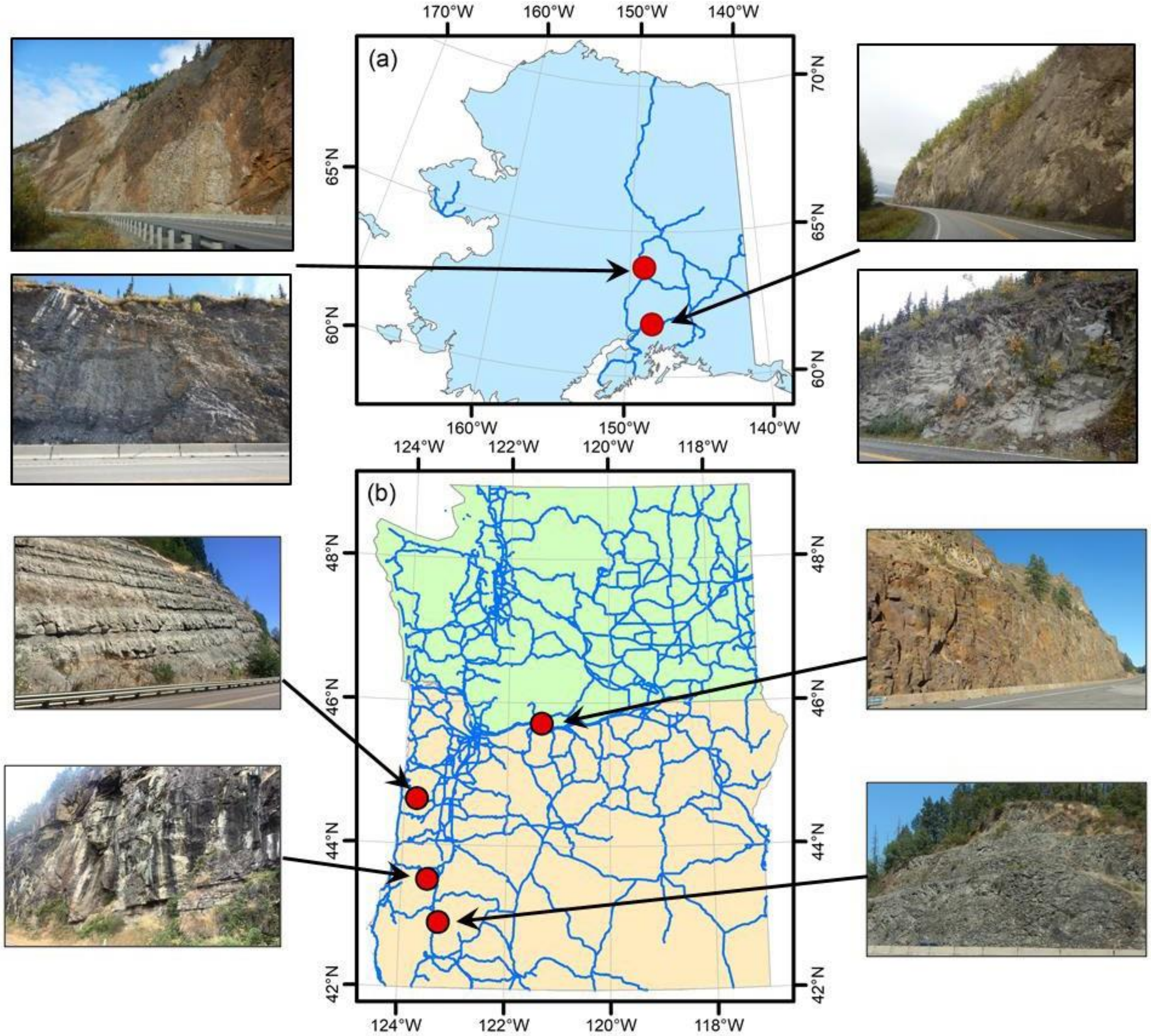

Figure 2.1 Field sites for lidar data collection and rock slope characterization. (a) ALASKA FIELD SITES: Examples of Nenana Canyon area, Parks Highway (left), and Long Lake area, Glenn Highway (right); (b) WASHINGTON/OREGON FIELD SITES (counterclockwise from middle right): Hewett Lake, Washington (State Route 14); Eddyville, Oregon (U.S. Route 20); Yellow Creek, Oregon (State Highway 138); Canyonville, Oregon (Interstate 5). In both map views, blue lines represent major roadways in each state; note that (a) is only a portion of Alaska. Base map imagery from ADOT&PF (2020), Alaska Geospatial Council (2020), Oregon Geospatial Enterprise Office (2023a and b), Washington Department of Natural Resources (2023a and b).

Figure 2.2 Acquisition of Schmidt hammer (SH) readings at sites in (a) Alaska and (b) Oregon.

At each site, we identified a minimum of ten SH testing locations along the rock slope face; all SH measurement locations were georeferenced. At each location, we constructed a grid of ten points within a 1-m^2 area. We developed an additional testing grid of ten points for locations where two individuals alternated taking measurements. The distance between each testing point on the grid was greater than 6 cm (2.36 in.) to prevent any overlap of deformation on the rock face. We took a measurement with each hammer type at each point, alternating which hammer type was used first at the different sites. If applicable, we noted the orientation to foliation or bedding because this can impact rebound values. For data analysis, we averaged all of the SH readings for each site, an approach that included effects of discontinuities in the rock mass. We also followed the ASTM D5873-14 standard, by averaging ten readings from a site, removing rebound values that differed from the average by seven or more, and then averaging the remaining values (ASTM 2014). Results from both approaches are included in this report.

Overall, we took 3,050 SH measurements at the Alaska sites, and 1,750 SH measurements at the Oregon and Washington sites. This report contains a summary of the typical testing grid results for selected Alaska sites and all of the Oregon and Washington sites. A companion PacTrans report by Herrman and Darrow (in review) provided an in-depth look into the SH testing, results, and preliminary results of unconfined compressive strength tests for rock samples from the Alaska sites.

2.2. Washington and Oregon Site Descriptions

2.2.1. Hewett Lake, Washington, State Route 14

The Hewett Lake site is located to the north of Washington State Route (SR) 14, which runs parallel to and north of the Columbia River. The study area is mapped as the middle Miocene Wanapum Basalt, Priest Rapids member (Twp; Korosec 1987). The bedrock at the highway level demonstrates the jointing pattern consistent with that of a lower colonnade, with a sharp transition to entablature, which forms the cliffs above the highway, indicating that this exposure is part of a Tertiary Columbia River flood basalt flow (Figure 2.3a). The basalt (dark gray when fresh and weathering to brown or brown-orange) contains abundant plagioclase (up to 1 mm long) and olivine in a gray groundmass. At the highway level, vertical columnar joints within the lower colonnade are prevalent. Additionally, several high angle faults (possibly normal, based on apparent offset) are present along the exposure. At the east end of the study site at elevations of ~ 59.2 m (~25 m above the current position of the Columbia River), we observed pockets of sand and rounded gravel on the surface of the basalt, sometimes nestled under overhanging blocks (Figure 2.3b). We interpreted these deposits to be remnants of the Missoula floods (Qfg; Korosec 1987), which occurred between 15,300 and 12,700 years ago. The presence of this gravel indicates that these blocks have been stable since the Last Glacial Maximum.

We conducted SH readings using both hammer types at ten locations at this site (see Table 2.1 for average results). We also made 214 measurements of discontinuities, including faults and joints (Figure 2.4). The road cut stands up to 80 m high at an ~80° maximum slope angle (facing ~200°). We noted the presence of several high angle faults (with average dip and dip direction of 86° and 99°, respectively), some of which we were able to estimate at 1.5 to 2 m of separation (Figure 2.3c, Figure 2.4).

Figure 2.3 Views of the Hewett Lake (SR 14) research site: (a) view to the east along the highway; (b) example of the interpreted Missoula flood deposits nestled under an overhanging block; (c) example of a high-angle fault.

Table 2.1 Summary of SH test results; R indicates rebound value.

Location	No. of sites	Rock type	L type, Avg. R		N type, Avg. R	
			All values	ASTM method	All values	ASTM method
ALASKA						
Long Lake (MP71)	10	Mudstone	29	29	31	31
Nenana Canyon (MP241)	10	Quartzite	41	42	42	42
WASHINGTON/OREGON						
Hewett Lake	10	Basalt	53	54	54	55
Eddyville	12	Sandstone	37	38	35	35
	2	Siltstone	0	0	1	0
Yellow Creek	10	Sandstone	43	43	41	42
	1	Siltstone	2	0	2	0
Canyonville	11	Tuff	28	31	28	29

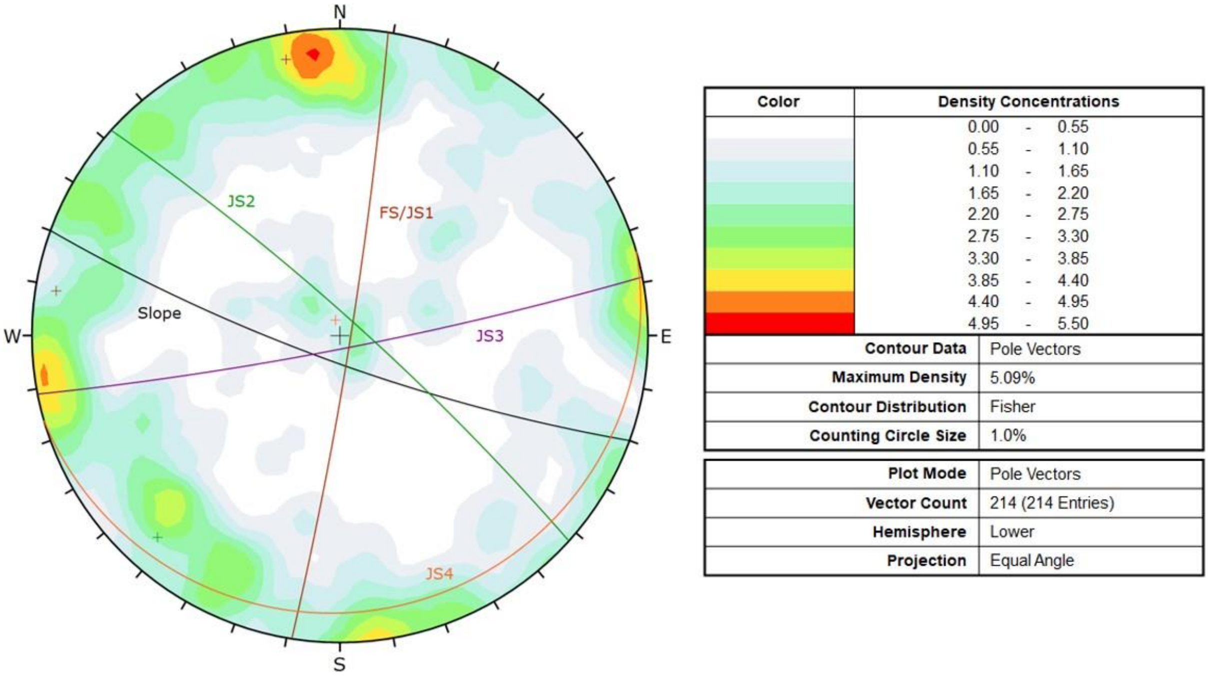

Color	Density Concentrations
⬜	0.00 - 0.55
⬜	0.55 - 1.10
🟦	1.10 - 1.65
🟦	1.65 - 2.20
🟩	2.20 - 2.75
🟩	2.75 - 3.30
🟩	3.30 - 3.85
🟨	3.85 - 4.40
🟧	4.40 - 4.95
🟥	4.95 - 5.50

Contour Data	Pole Vectors
Maximum Density	5.09%
Contour Distribution	Fisher
Counting Circle Size	1.0%

Plot Mode	Pole Vectors
Vector Count	214 (214 Entries)
Hemisphere	Lower
Projection	Equal Angle

Figure 2.4 Stereonet for Hewett Lake, Washington (SR 14).

2.2.2. Eddyville, Oregon, U.S. Route 20

The Eddyville site is one of several rock cuts associated with a recent realignment along U.S. Route 20. The specific location we scanned in 2022 is located on the north side of the highway and, at its highest, is ~27 m high at a ~65° maximum slope angle (facing ~180°). The bedrock is mapped as the middle Eocene Tyee Formation, which formed as turbidites (Tt; Snavely et al. 1976). The exposure consists of repeating beds of light gray, friable, medium-grained micaceous lithic graywacke fining upwards to dark gray micaceous siltstone (Figure 2.5a and b). Some beds contain lenses of siltstone within the wacke, and black plant fossils and laminae are often present within the upper portions of each bed. Where measured, beds range in thickness from 0.6 m to 3.4 m (with siltstone ranging from 8 cm to 30 cm thick, and wacke typically ranging from 0.65 m to 2 m thick; Figure 2.5c). We observed water seeping out of the rock cut along several of the siltstone exposures despite the dry conditions and a ~32°C temperature (Figure 2.5b), and we also witnessed some of this moist to wet rock collapsing downslope in cm-thick plates. Other evidence of the persistent presence of water is iron staining within the siltstone. The wacke, although friable, typically forms overhangs above the recessed siltstone portion of the underlying bed.

We took 31 measurements of bedding, joints, and faults. The high-angle normal faults form notable drainages in the topography above the rock cut, providing preferential flow paths for water, with larger debris piles forming at their base. Some of these faults were obscured with vegetation, which was likely growing where there was more available water (Figure 2.5d). Measured displacements ranged from only 1 cm to 0.7 m offset, with some faults containing black gouge and iron staining. One fault demonstrated apparent strike-slip movement based on the orientation of slickens on the fault surface. Figure 2.6 is the stereonet for this location, displaying the consistent bedding (avg. dip and dip direction of 14°/335°) and predominate fault/joint set (avg. dip and dip direction of 82°/88°). We also conducted SH readings using both hammer types at 12 locations for the graywacke parallel with bedding, and at two locations for the siltstone parallel with bedding (see Table 2.1 for average results). The values presented in Table 2.1 for siltstone represent one non-zero reading for the N-type SH; all other readings for the siltstone were 0. These results agreed with the visual observations of the siltstone being the weaker of the two types of rock exposed.

Figure 2.5 Photographs of the geology at the Eddyville research site: (a) view to the east along the highway; (b) example of overhanging greywacke underlain by siltstone with evidence of water seepage; (c) measuring bed thickness at an SH measurement site; (d) high-angle, normal fault with vegetation.

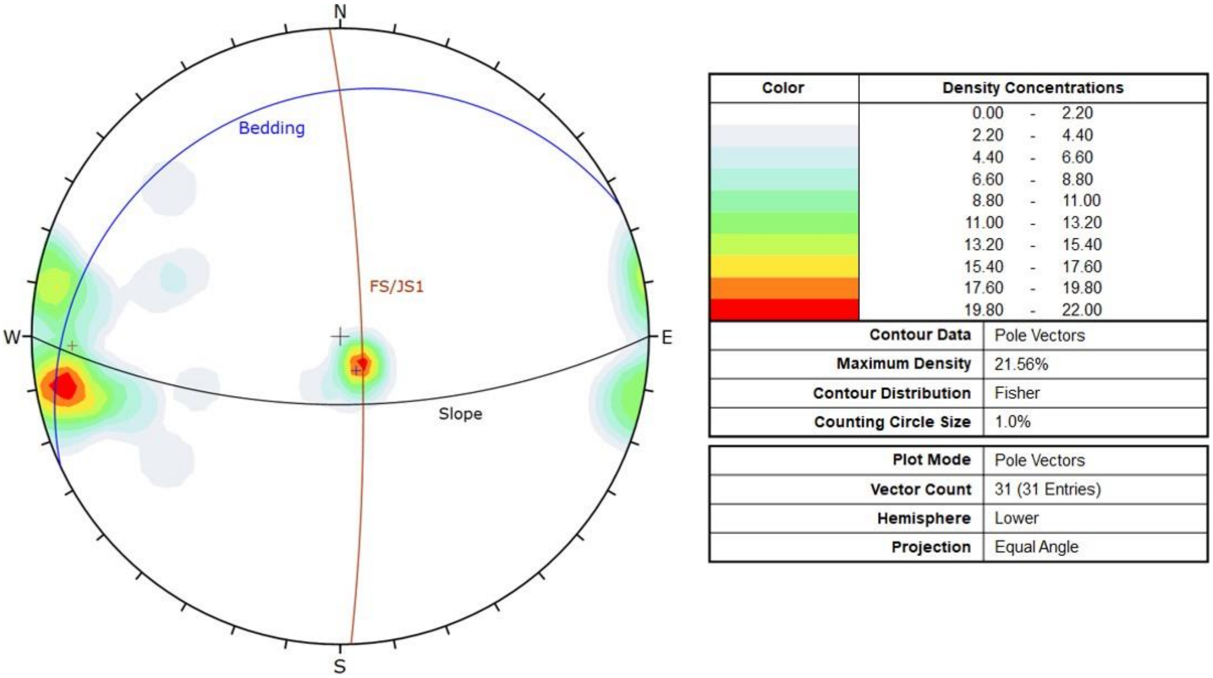

Figure 2.6 Stereonet for Eddyville, Oregon (U.S. Route 20).

2.2.3. Yellow Creek, Oregon, State Highway 138

The investigated road cut is immediately to the north of Oregon State Highway 138, in an area mapped as part of the Baughman Lookout Member of the middle Eocene Tyee formation (Tet3; Niem and Niem 1990). The bedrock consists of thick (sometimes > 30-m) beds of medium- to coarse-grained, lithic, micaceous sandstone to wacke (Figure 2.7a), and sequences of interbedded siltstone and sandstone.

The sandstone, light gray when fresh and weathering to dark gray to black, sometimes contains lenses of siltstone and demonstrates bedding with layers of fossilized plant fragments (1 cm by 15 cm) on which it breaks (Figure 2.7b). The fine-grained layers consist of dark gray siltstone with interbeds of fine-grained sandstone demonstrating laminae. We observed ripple marks (~0.5 m wide) in one sample at the contact between the siltstone and coarse-grained sandstone.

We took 45 measurements of bedding, joints, and faults along this slope, which is up to 47 m high at a ~85° maximum slope angle (generally facing 210°). As with the Eddyville site, bedding is prominent, although with a different orientation (avg. dip and dip direction of 10°/287°). The site also contains a conjugate set of high angle faults (Figure 2.7c and Figure

2.8), some demonstrating measurable offset. We also conducted SH readings using both hammer types at ten locations for the sandstone parallel with bedding, and at one location for the siltstone, also parallel with bedding (see Table 2.1 for average results). The values presented in Table 2.1 for siltstone represent one non-zero reading for both the L-type and N-type hammers; all other readings for the siltstone were 0.

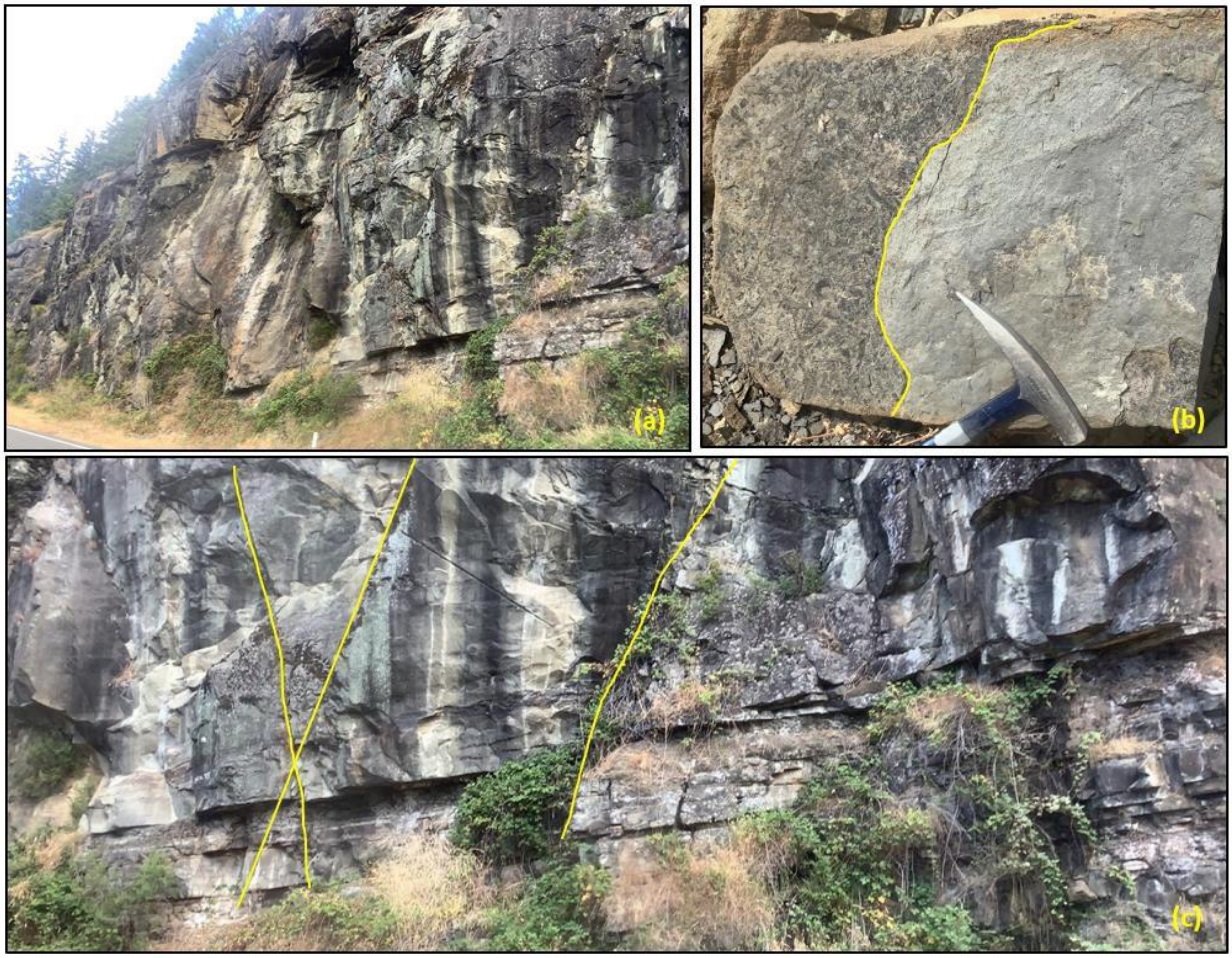

Figure 2.7 Views of the geology at the Yellow Creek research site: (a) looking at the outcrop to the north of the highway; (b) annotated view of sandstone boulder with a layer rich in leaf fossils (left of yellow line) on which the sandstone layers (right of yellow line) fracture; and (c) annotated view of high angle faults (yellow lines) with measurable offset.

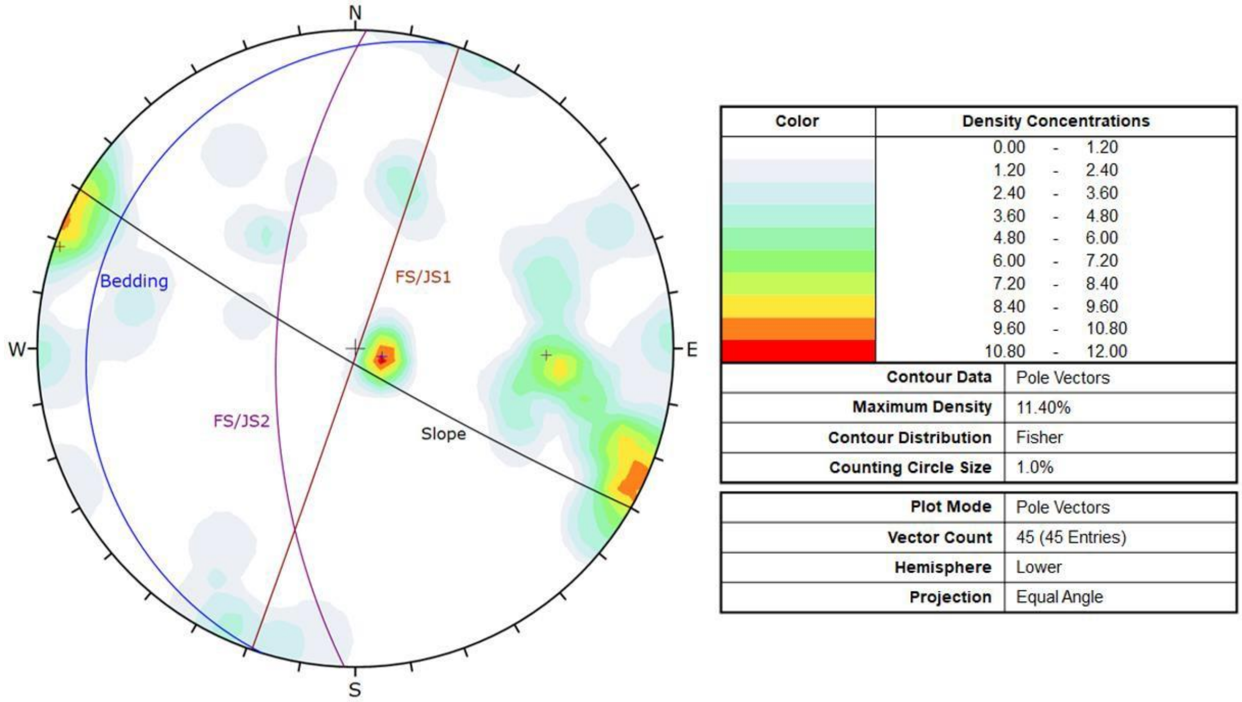

Color	Density Concentrations
⬜	0.00 - 1.20
⬜	1.20 - 2.40
🟦	2.40 - 3.60
🟩	3.60 - 4.80
🟩	4.80 - 6.00
🟩	6.00 - 7.20
🟩	7.20 - 8.40
🟨	8.40 - 9.60
🟧	9.60 - 10.80
🟥	10.80 - 12.00

Contour Data	Pole Vectors
Maximum Density	11.40%
Contour Distribution	Fisher
Counting Circle Size	1.0%

Plot Mode	Pole Vectors
Vector Count	45 (45 Entries)
Hemisphere	Lower
Projection	Equal Angle

Figure 2.8 Stereonet for Yellow Creek, Oregon (State Highway 138).

2.2.4. Canyonville, Oregon, Interstate-5

The investigated road cut is east of Interstate-5, in an area mapped as massive tuffs and agglomerates (Jpta; Johnson and Page 1979) (Figure 2.9). The bedrock is a tuff consisting of clear to milky white plagioclase up to 4 mm long and rare lapilli up to 8 mm long in a light gray-green matrix, weathering to dark gray to black. The measured slope, which is cut into two benches, has an overall height of 55 m (lower bench ~18.9 m high and middle bench ~16.8 m high) at a 70° maximum slope angle (facing 225°). A local ODOT employee indicated that the maintenance crew cleans the ditch below the cut (constructed around 1965) every year; however, the employee was not aware of any cleaning along the benches (B. Coffland, pers. comm., August 2022). We collected 212 measurements of faults and joints, taken along the base of the slope and along the first bench. The rock mass is highly fractured, containing four sets of discontinuities, two of which consist of both faults and joints (Figure 2.10). We conducted SH readings using both hammer types at 11 locations (see Table 2.1 for average results).

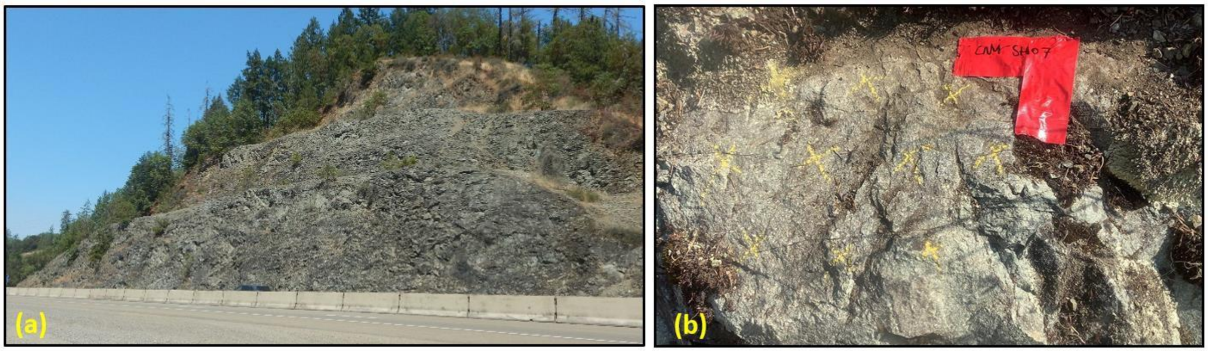

Figure 2.9 Views of Canyonville research site: (a) looking north across Interstate-5 at the measured slope; (b) a close-up view of a SH reading location on the tuff.

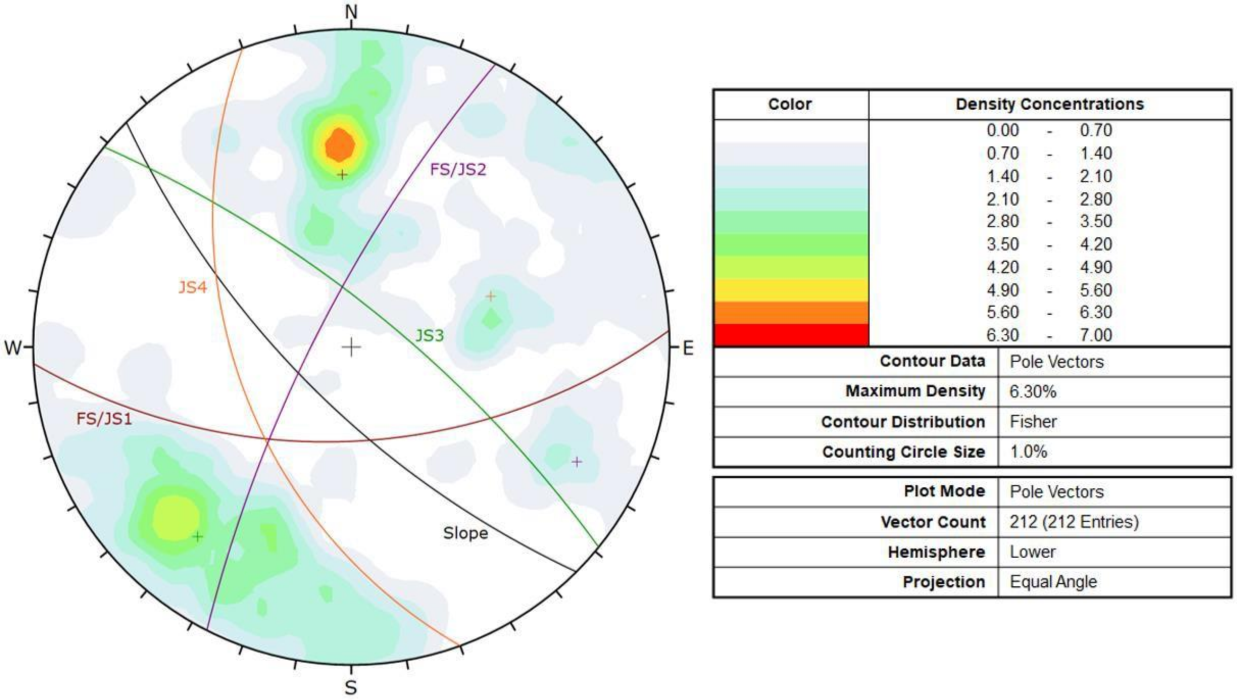

Color	Density Concentrations
⬜	0.00 - 0.70
⬜	0.70 - 1.40
🟦	1.40 - 2.10
🟦	2.10 - 2.80
🟩	2.80 - 3.50
🟩	3.50 - 4.20
🟩	4.20 - 4.90
🟨	4.90 - 5.60
🟧	5.60 - 6.30
🟥	6.30 - 7.00

Contour Data	Pole Vectors
Maximum Density	6.30%
Contour Distribution	Fisher
Counting Circle Size	1.0%

Plot Mode	Pole Vectors
Vector Count	212 (212 Entries)
Hemisphere	Lower
Projection	Equal Angle

Figure 2.10 Stereonet for Canyonville, Oregon (Interstate-5).

2.3. Mapping Major Discontinuities

In addition to the hands-on measurements, research team members made small-scale observations of each individual slope cut while in the field. These included identifying major discontinuities (likely faults), contacts between different rock units, and areas of notable water seepage. Once back from the field, we transferred those observations onto compilations of highresolutions photographs taken via UAS or on the ground (in one case). Figures 2.11 through 2.17 illustrate these small-scale features (i.e., large discontinuities) for selected research locations.

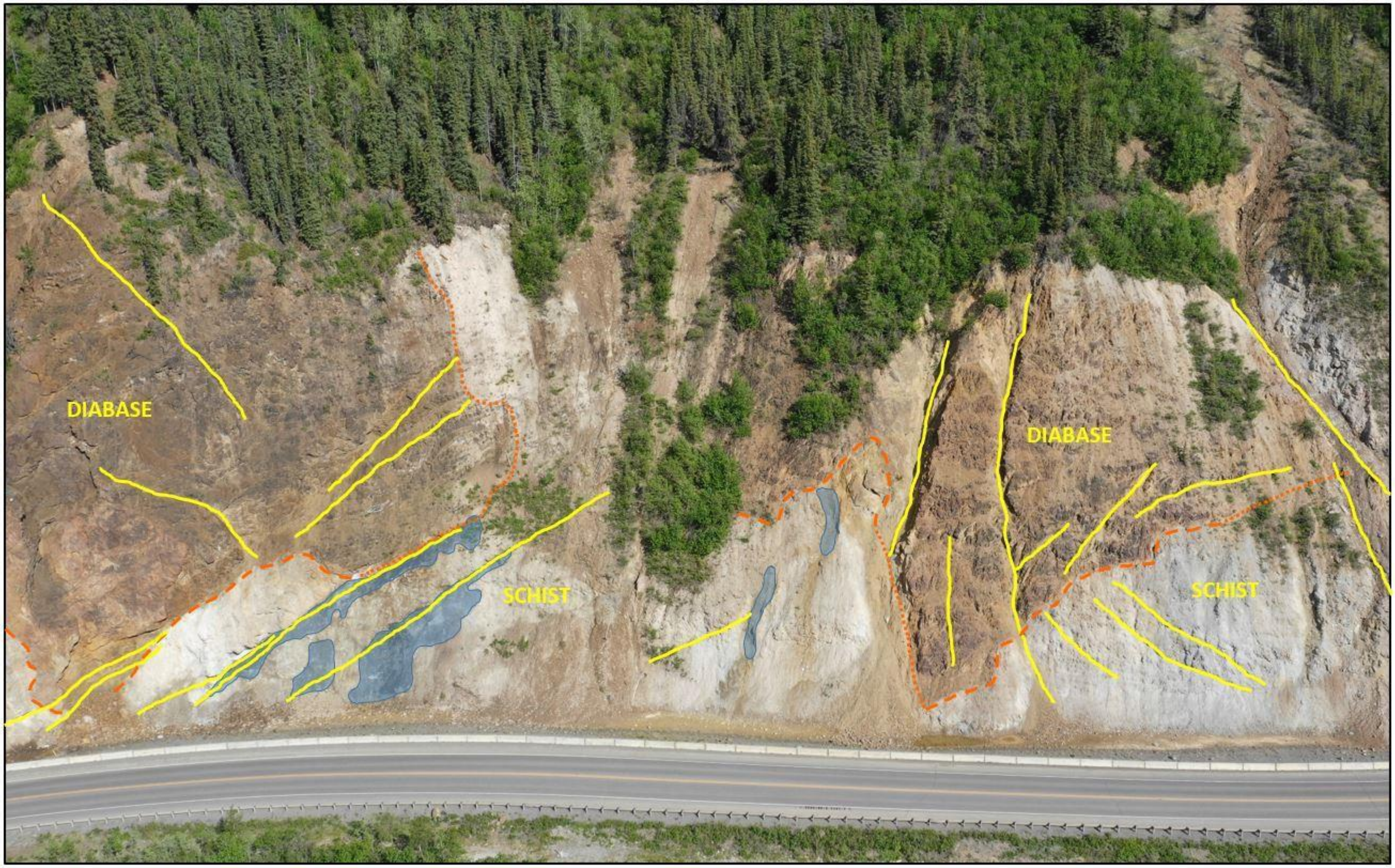

Figure 2.11 Nenana Canyon (MP 239), Alaska: major discontinuities (yellow), contacts between rock units (orange, dashed where observed, dotted where covered), and water seepage areas (blue).

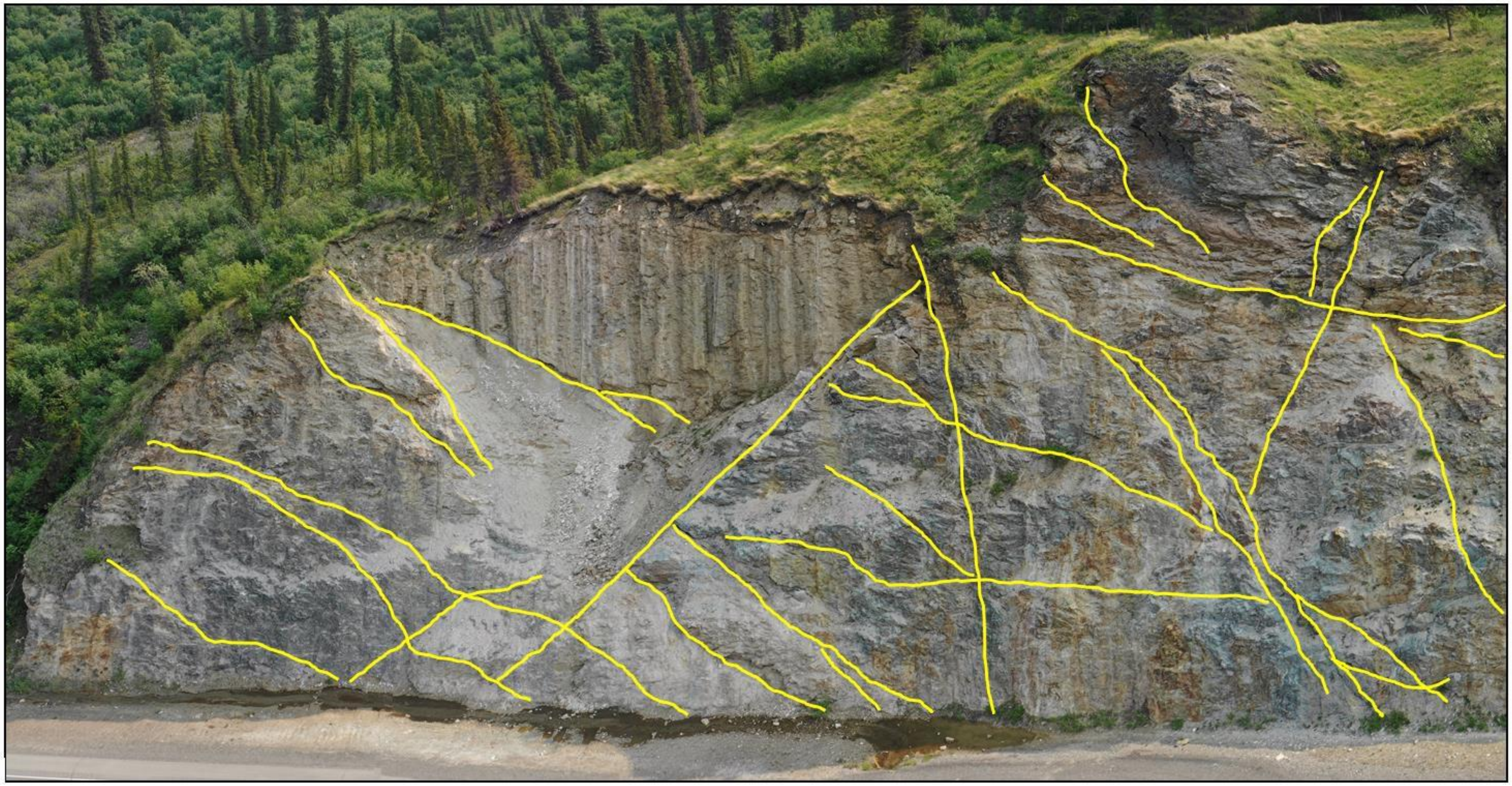

Figure 2.12 Nenana Canyon (MP 241), Alaska, north section: major discontinuities (yellow) in micaceous quartzite and muscovite/sericite quartz schist.

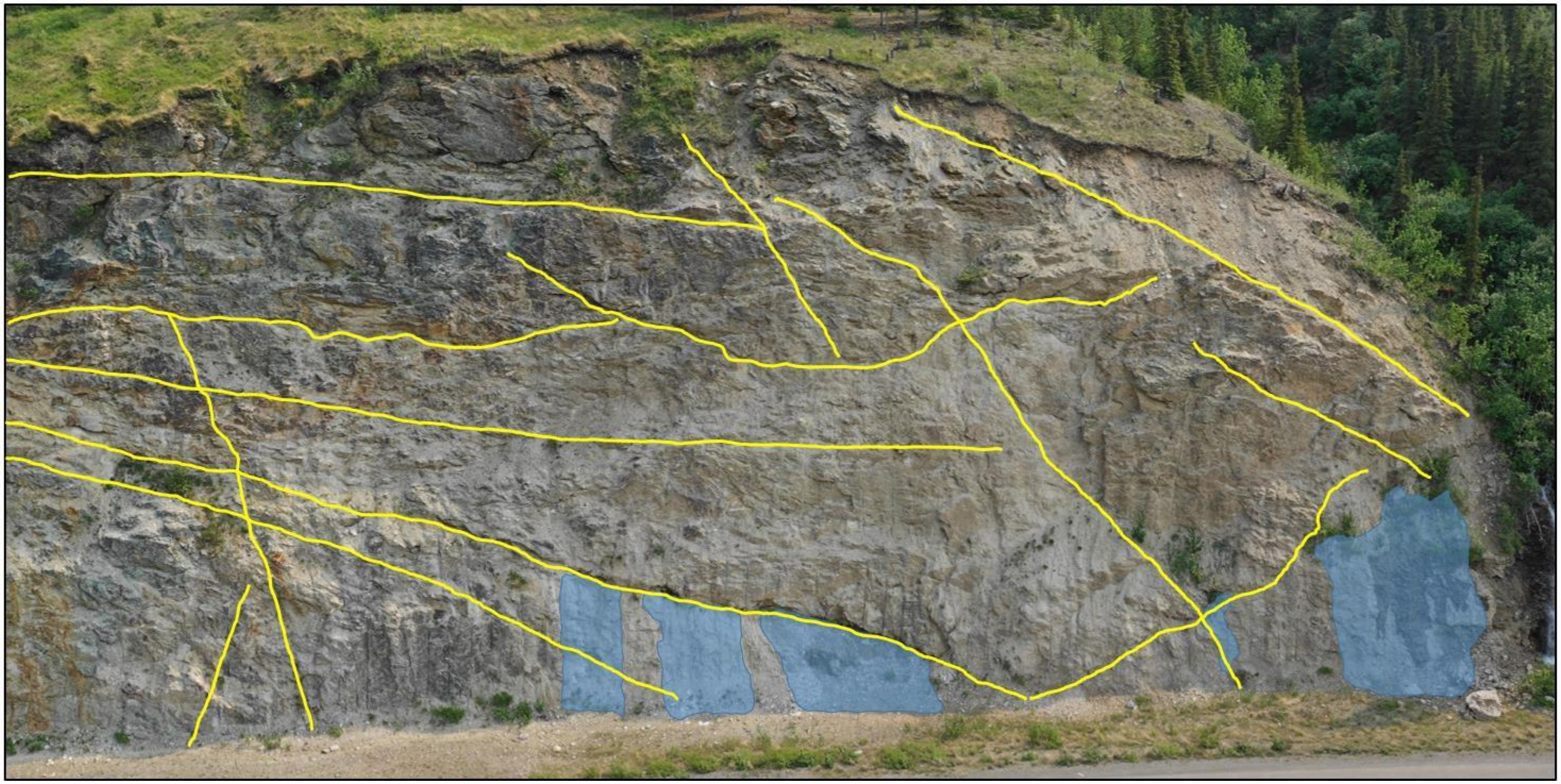

Figure 2.13 Nenana Canyon (MP 241), Alaska, south section: major discontinuities (yellow) and water seepage areas (blue) in micaceous quartzite and muscovite/sericite quartz schist.

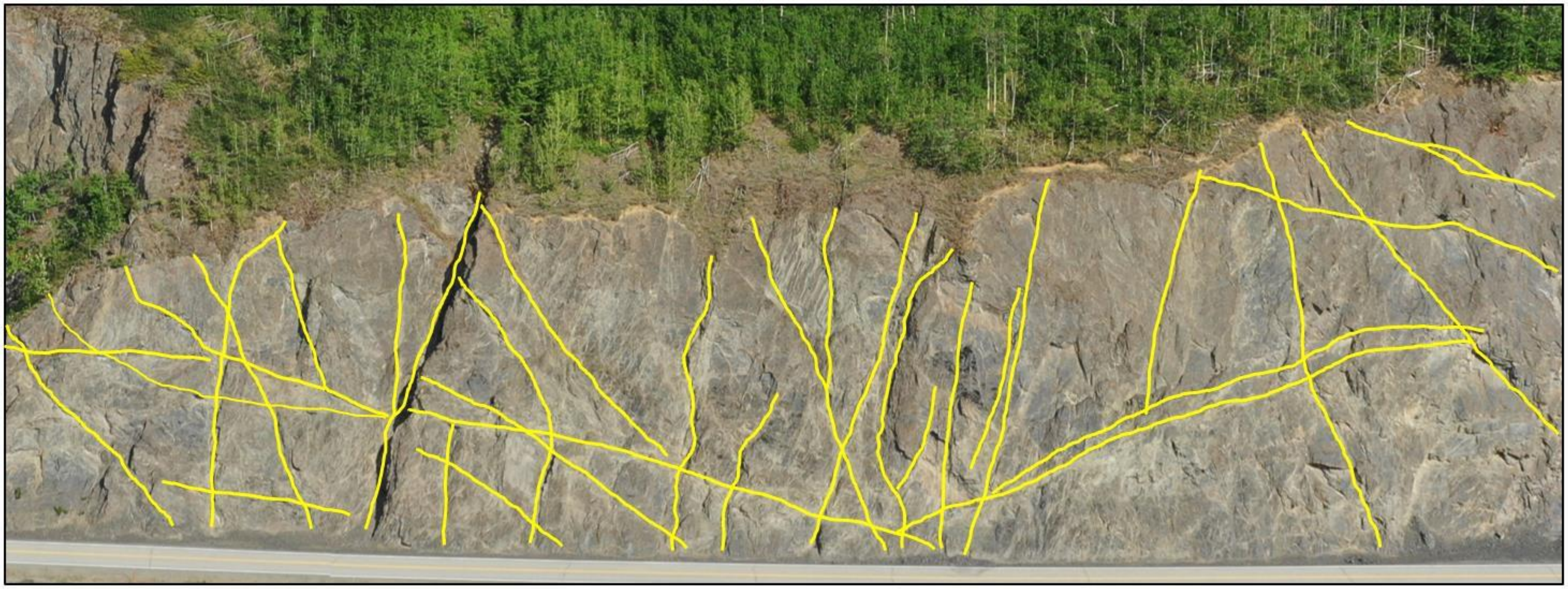

Figure 2.14 Long Lake (MP 71), Alaska, west section: major discontinuities (yellow) in mudstone.

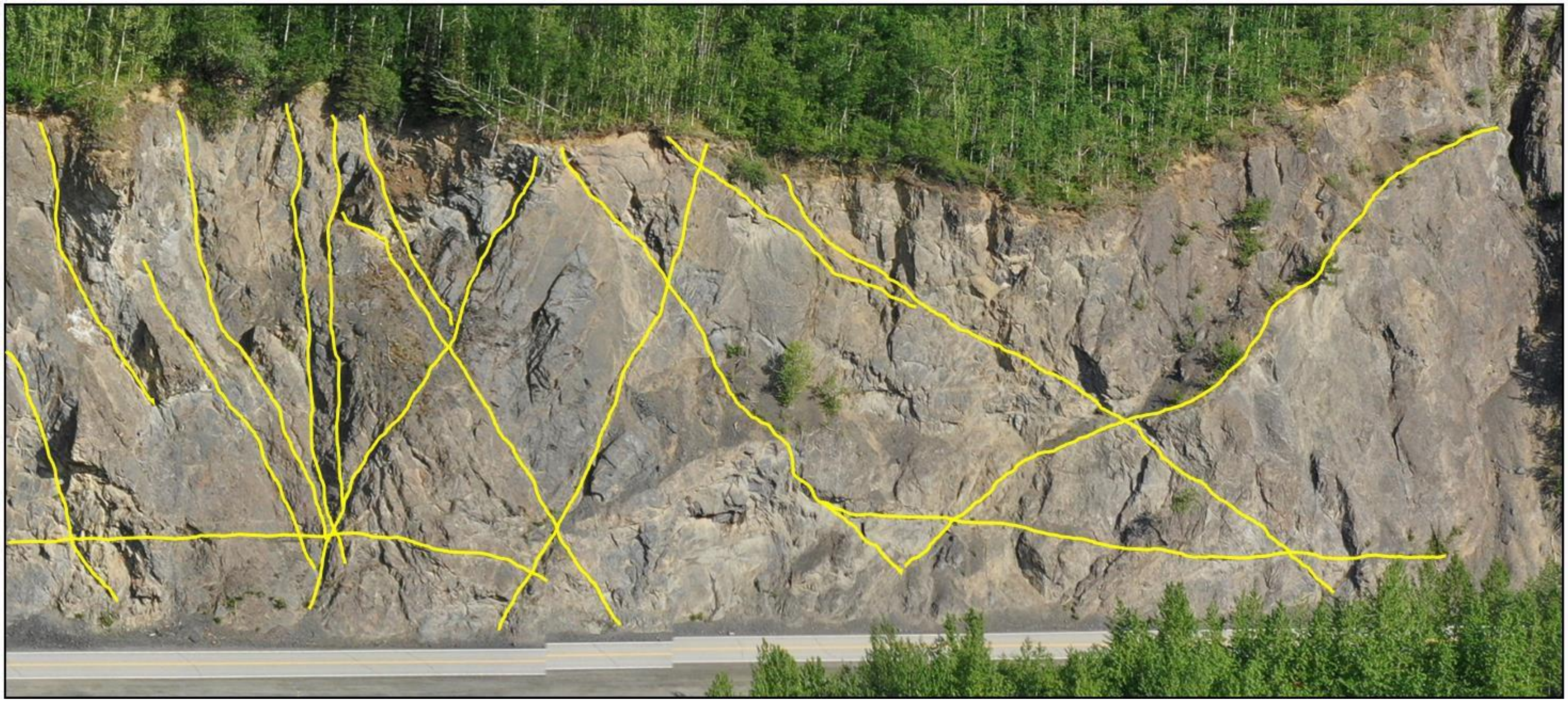

Figure 2.15 Long Lake (MP 71), Alaska, east section: major discontinuities (yellow) in mudstone.

Figure 2.16 Eddyville, Oregon: major discontinuities (yellow) and water seepage areas (blue) in alternating beds of greywacke and siltstone (rose lines mark the bottom of each greywacke bed). Note that this image covers only the extreme east end of the site.

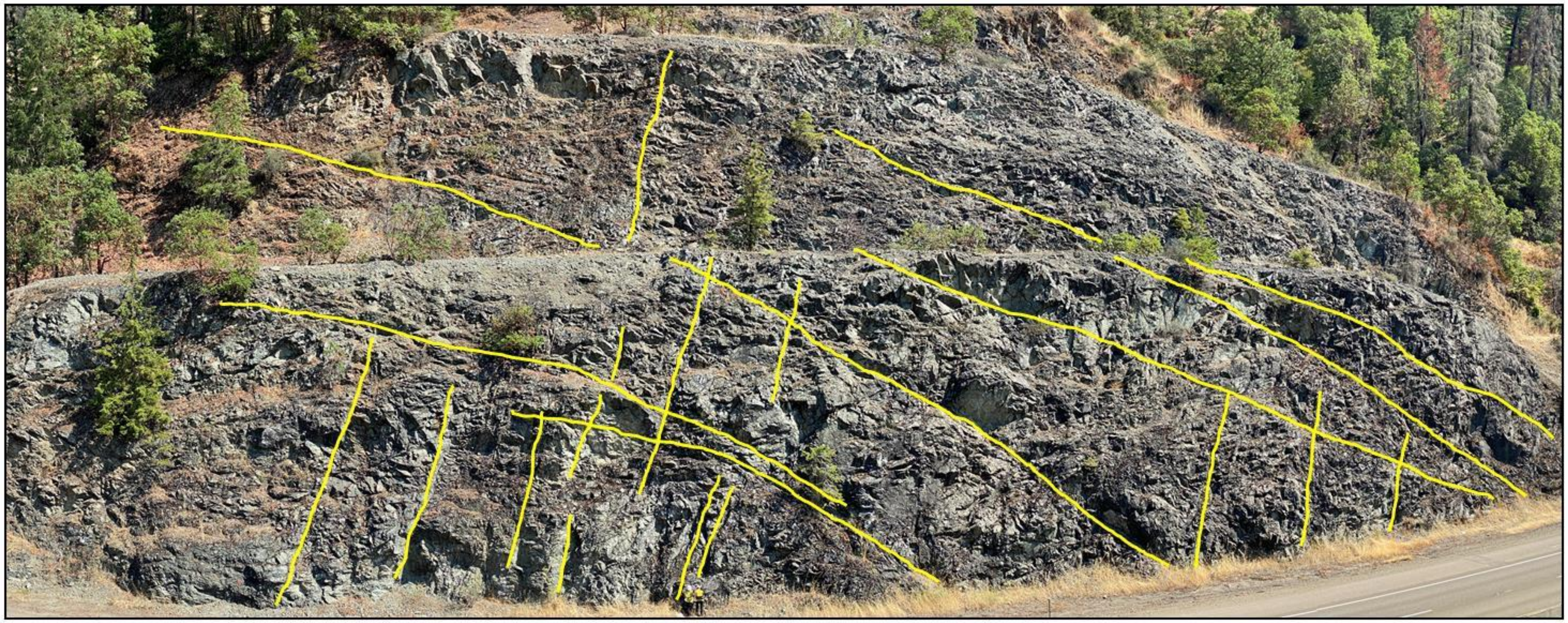

Figure 2.17 Canyonville, Oregon: major discontinuities (yellow) in tuff.

CHAPTER 3. DATA ANALYSIS

3.1. Comparison of Schmidt Hammer (SH) Data to Rockfall Rates

Although SH data were collected at all of the field sites, we selected the same four sites for data analysis for which we presented images of the major discontinuities in Section 2.3: Nenana Canyon MP 241 (NC241); Long Lake MP 71 (LL71); Eddyville (EV); and Canyonville (CV). Each of these sites has different geologic conditions and consequently variable structural controls for rockfall activity. Our initial evaluation of the data led us to remove the EV data from the analysis because the prominent bedding at this location controls the rockfall mechanism (i.e., raveling of siltstone beds undermines the wacke, causing cantilevered blocks to fall). We did not expect this rockfall process to be reflected by the specific rebound values from SH measurements.

The georeferenced location of each SH measurement site enabled our analysis of inter-epochal failure rates (f_i) of the surrounding area. To determine f_i values (measured in m), we calculated the mean erosion rate within a 1-m Euclidean radius around the SH site. These erosion values became rates by dividing retreat of the rock face by the time interval between lidar collections. Through this process, we calculated a single, median time-normalized failure rate (f) and its percentiles based on all individual failure rates measured at a given location. We performed this calculation for each SH measurement location, which allowed the systematic comparison of the relationship between SH measurements and overall erosional rockfall activity. At some locations, SH measurement sites happened to be placed within occlusions or data gaps where erosional activity could not be measured; we did not include these measurements. Here, we describe some of the observed relationships between failure rates and SH measurements, including 1) median uncorrected SH measurements; 2) median corrected SH measurements (per ASTM standard (ASTM 2014)); and 3) mean corrected SH measurements.

3.1.1. Relationships between Uncorrected SH Measurements and f

The data presented in Figure 3.1 illustrate the relationships between the uncorrected median SH measurements and f. There was considerable variability in both uncorrected median SH measurements and f for each of the three analyzed sites; however, an inverse relationship existed between uncorrected SH measurements and f. Lower uncorrected median SH measurements generally reflected higher overall failure rates. This observation suggests that for these three locations (each having a completely different geology), the SH readings, even when uncorrected, could be used as a proxy for potential erosion of rock slopes at the measurement locations. We fit power-law relationships to these data, as there were several orders of magnitude deviation in failure rates; testing also indicated that these fits provided the best goodness-of-fit outputs (Table 3.1). As demonstrated by the modest R^2 values, however, there was significant variability in these relationships. All sites generally demonstrated decreasing SH rebound values with *f* values, and relationships where the failure rate was predicted as a function of SH measurements (Figure 3.1b) had better goodness-of-fit than the reverse trends. Some sites demonstrated better trends (e.g., LL71), and overall relationships were reasonable; however, the significant scatter suggested that a more in-depth analysis was required to evaluate uncertainty.

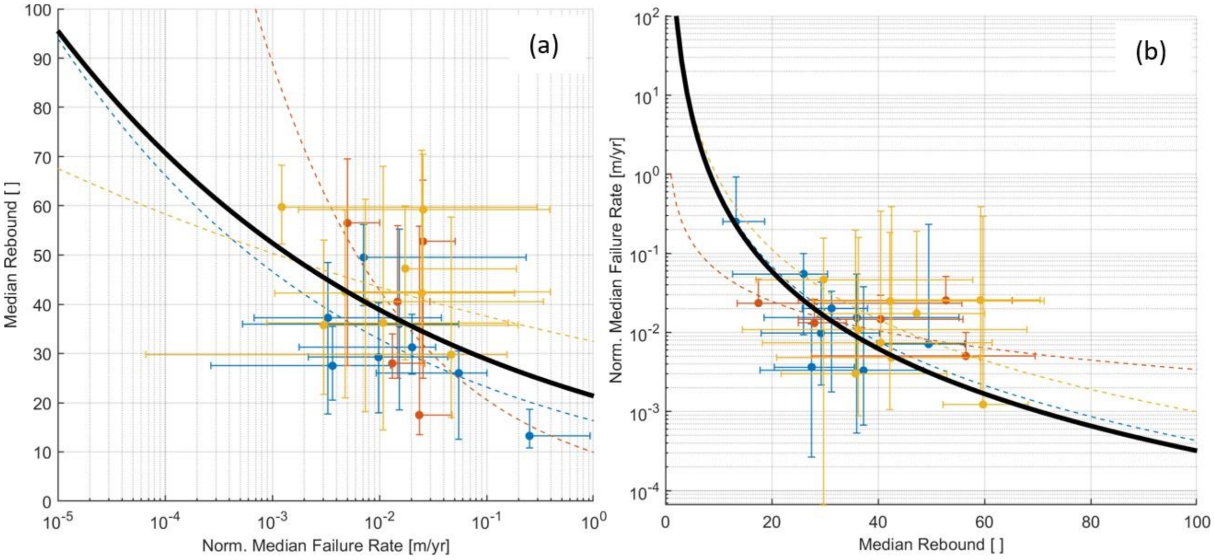

Figure 3.1 Comparison of uncorrected SH measurements with normalized failure rates: (a) median uncorrected SH rebound values versus normalized median failure rates (m yr^{-1}) and (b) normalized median failure rates (m yr^{-1}) versus median uncorrected SH rebound values. For both graphs, yellow is NC241, blue is LL71, and red is CV. Whiskers reflect the 10th and 90th percentiles for each data point; colored lines reflect power-law fits for each site; and the bold black line represents the power-law relationship for all sites. Note: the power-law fits and goodness-of-fit for both plots are presented in Table 3.1.

Table 3.1 Power-law relationships between median uncorrected SH rebound values and normalized median failure rates (m yr^{-1}) and goodness-of-fit for each site and all sites.

Site	Median Uncorrected Rebound	R^2	Median Failure Rate (m yr^{-1})	R^2
NC241	$S = 32.41f^{-0.06}$	0.10	$f = 752.6S^{-2.94}$	0.25
LL71	$S = 16.32f^{-0.15}$	0.43	$f = 868.4S^{-3.15}$	0.89
CV	$S = 9.90f^{-0.32}$	0.25	$f = 1.1S^{-1.23}$	0.21
All	$S = 21.34f^{-0.13}$	0.22	$f = 998.1S^{-3.24}$	0.83

3.1.2. Relationships between Corrected SH Measurements and Normalized Failure Rates

The data in Figure 3.2 illustrate the relationships between corrected median SH measurements and *f*. Similar to the uncorrected data in Figure 3.1, there was considerable variability in both corrected median SH measurements and *f*. There were slight differences between corrected and uncorrected SH values. Typically, corrected values were higher; however, differences were modest. Similar to the uncorrected SH measurements, an overall inverse relationship existed between corrected SH measurements and *f*, where lower corrected median SH measurements generally had higher overall failure rates. We fit power-law relationships to these data (see Table 3.2). Again, as demonstrated by the modest R^2 values, there was significant variability in these relationships; however, all R^2 values associated with power-law fits for SH vs. *f* were equal or better than those based on uncorrected SH measurements. For example, CV had an R^2 of 0.85 with the corrected data, as opposed to an R^2 of 0.25 with the uncorrected data. Uncorrected data appeared to perform better for *f* vs. SH, although the significance of this observation was debatable given the limited analysis. That said, the R^2 for the overall corrected relationship (Table 3.2) was nearly equivalent to that for the uncorrected relationship (Table 3.1). Once again, all sites generally demonstrated decreasing SH with *f* values. The modest improvement in the proposed relationships suggested that correcting SH measurements per the ASTM standard could be beneficial.

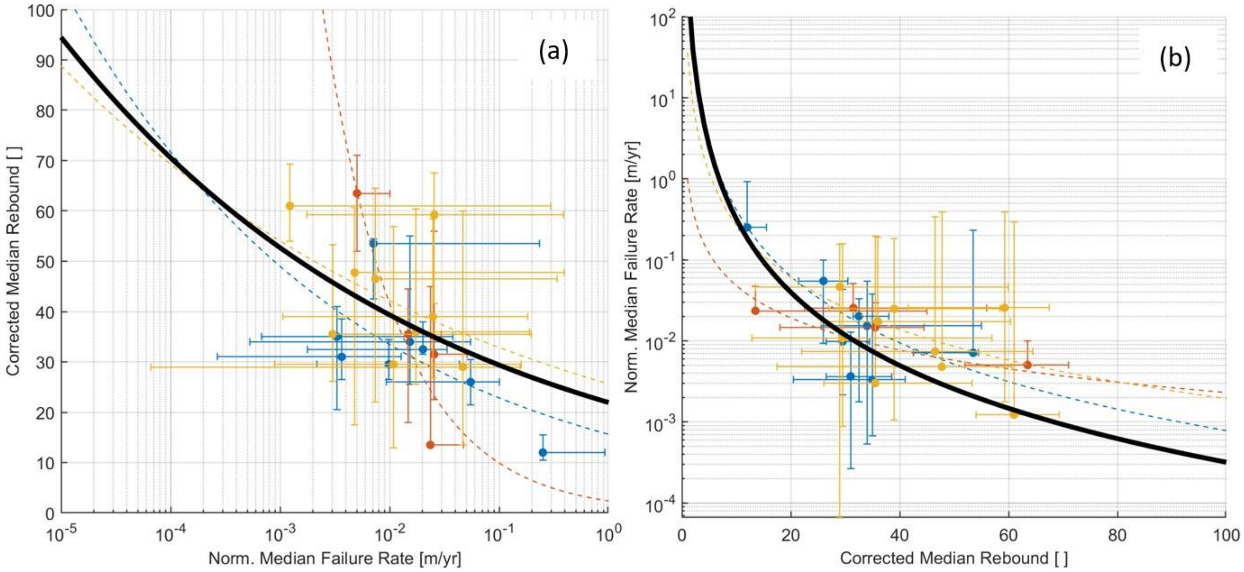

Figure 3.2 Comparison of corrected SH measurements with normalized failure rates: (a) median corrected SH rebound values versus normalized median failure rates (m yr^{-1}) and (b) normalized median failure rates (m yr^{-1}) versus median corrected SH rebound values. For both graphs, yellow is NC241, blue is LL71, and red is CV. Whiskers reflect the 10th and 90th percentiles for each data point; colored lines reflect power-law fits for each site; and the bold black line represents the power-law relationship for all sites. Note: the power-law fits and goodness-of-fit for both plots are presented in Table 3.2.

Table 3.2 Power-law relationships between median corrected rebound and normalized median failure rate (m yr^{-1}) and goodness-of-fit for each site and overall sites.

Site	Median Corrected Rebound	R^2	Median Failure Rate (m yr^{-1})	R^2
NC241	$S = 25.62f^{-0.11}$	0.10	$f = 37.1S^{-2.14}$	0.20
LL71	$S = 15.62f^{-0.17}$	0.44	$f = 218.2S^{-2.72}$	0.87
CV	$S = 2.36f^{-0.62}$	0.85	$f = 1.3S^{-1.32}$	0.26
All	$S = 21.93f^{-0.12}$	0.22	$f = 318.6S^{-2.98}$	0.65

3.1.3. Relationships between Corrected Mean SH Measurements and Normalized Median Failure Rates

The data presented in Figure 3.3 illustrate the relationships between mean corrected SH measurements and *f*. Mean corrected SH measurements tended to be higher than median values, suggesting that the distribution of SH readings, regardless of correction, were log-normal. Similar to previous comparisons, an overall inverse relationship existed between mean corrected

SH measurements and *f*, where lower mean corrected SH measurements generally reflected higher overall failure rates. We fit power-law relationships to these data; as with the previous analyses, the power-law fits provided the best goodness-of-fit outputs (Table 3.3). There was significant variability in these relationships, but all fits were notably improved in comparison to those with the corrected and uncorrected median SH measurements. Once again, all sites generally demonstrated decreasing SH with *f* values, and decreasing *f* with SH measurements. The notable improvement in these relationships suggested that correcting SH measurements per the ASTM standard could be beneficial, and mean corrected SH measurements tended to demonstrate better behavior than median values.

Hence, these results suggested that analysis of a larger data set might improve the trends.

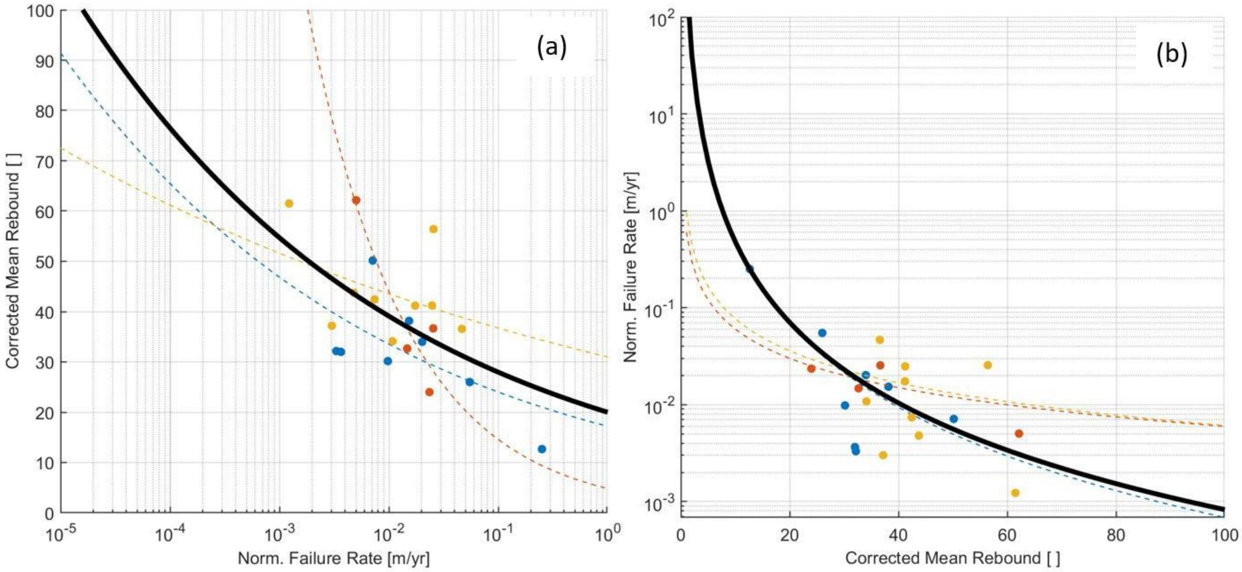

Figure 3.3 Comparison of mean corrected SH measurements with normalized median failure rates: (a) mean corrected SH rebound values versus normalized median failure rates (m yr^{-1}) and (b) normalized median failure rates (m yr^{-1}) versus mean corrected SH rebound values. For both graphs, yellow is NC241, blue is LL71, and red is CV. Whiskers reflect the 10th and 90th percentiles for each data point; colored lines reflect power-law fits for each site; and the bold black line represents the power-law relationship for all sites. Note: the power-law fits and goodness-of-fit for both plots are presented in Table 3.3.

Table 3.3 Power-law relationships between median corrected rebound and normalized median failure rate (m yr^{-1}) and goodness-of-fit for each site and overall sites.

Site	Median Corrected Rebound	R^2	Median Failure Rate (m yr^{-1})	R^2
NC241	$S = 31.00f^{-0.07}$	0.16	$f = 0.97S^{-1.10}$	0.09
LL71	$S = 17.19f^{-0.15}$	0.41	$f = 356.2S^{-2.87}$	0.88
CV	$S = 4.83f^{-0.48}$	0.85	$f = 0.61S^{-1.04}$	0.54
All	$S = 20.00f^{-0.15}$	0.31	$f = 279.2S^{-2.76}$	0.89

3.1.4. Practice-Based Modifications to the RAI Activity Rates

As noted in Section 3.1.1, analysis of the field data suggested that even uncorrected SH measurements might be used as a proxy for rock slope erosion or “failure” at the study sites. Moreover, we found that correcting the SH readings provided an even stronger correlation between SH and failure rate in close proximity to the hammer measurements locations. Accordingly, we developed a revised approach for identifying RAI input parameters and conducting a hotspot analysis.

When initially formulating the RAI system, Dunham et al. (2017) suggested an approximate range of RAI activity rates for each morphological classification based on observations of several rock slopes in Alaska over a one-year period. Subsequently, Markus (2018) assessed a more comprehensive morphological change analysis in these same rock slopes over a four-year period. Figure 3.4 is a graphical presentation of Markus’ (2018) analysis aggregated across all sites for Long Lake (LL) and all observation years. The figure presents box-and-whisker plots representing ranges of observed activity rates and those suggested by Dunham et al. (2017). Because the observed long-term annual activity rates were generally higher than those initially recommended in 2017, Markus (2018) suggested increasing activity rates, as noted in Table 3.4. Additionally, Markus (2018) reported a discrepancy in the threshold angle used to classify talus morphologically. Specifically, he found that some sites were erroneously classified as occurring in intact rock when they occurred in talus, and the suggested modifying the threshold angle from 35° to 42°. Adopting these improved modified parameters would change the hotspot mapping, as indicated in Figure 3.5. We recommend that the activity values suggested by Markus (2018) serve as the baseline parameters for RAI analysis.

The relationships presented in Figure 3.3 revealed a threshold-type relationship between mean corrected SH rebound values and normalized rock slope failure rates. Specifically, SH values of 20 or less were associated with high failure rates. At lower SH values (i.e., SH < 20), we recommend adopting the upper range of interquartile failure rate values presented in Figure 3.4 for analysis. For example, if obtaining SH values less than 20 in an area of 10-cm discontinuities, select a failure rate of ~0.10 (Figure 3.4) rather than the mean of 0.0306 (Table 3.4). In all cases, the higher activity rate value for talus (i.e., eroded material) should be used in the RAI analysis (i.e., talus activity rate of 0.129; Table 3.4).

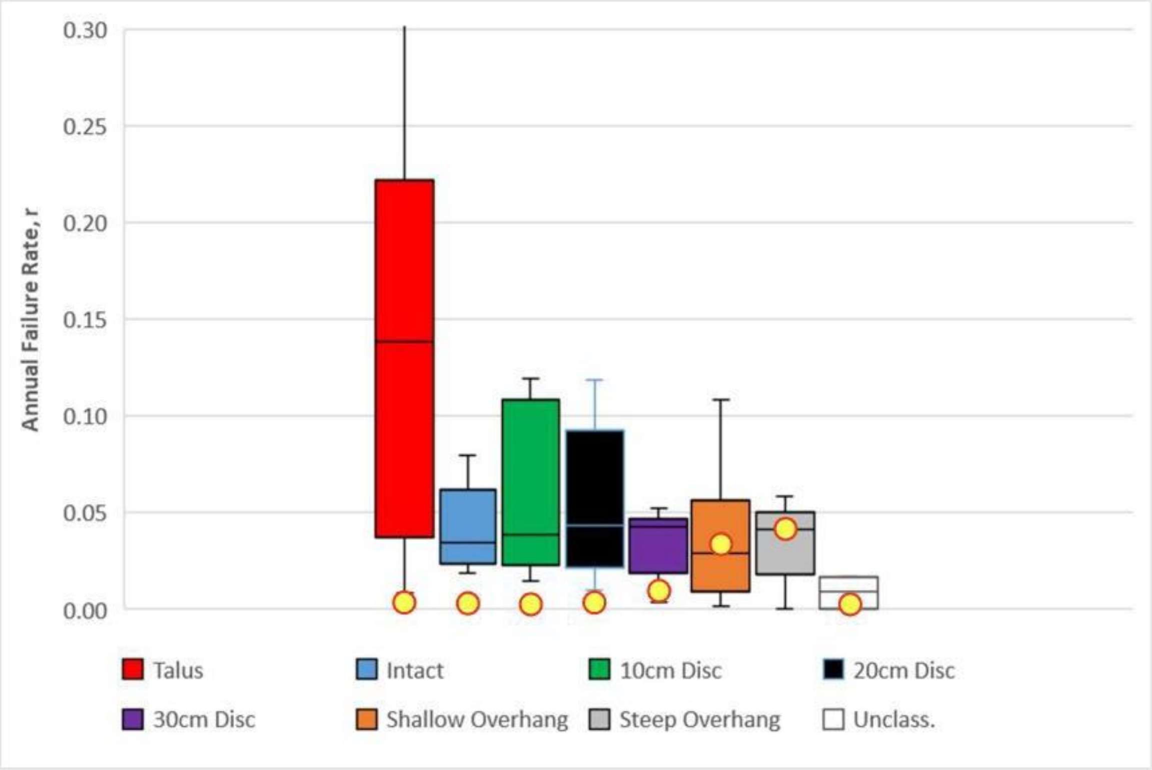

Figure 3.4 "Box-and-whiskers" plot showing the range of failure rates for each morphological class at Long Lake, Alaska, study sites over a four-year period (Markus, 2018). Plot shows interquartile range (colored boxes) along with extreme values (whisker portion). The yellow dots indicate mean values initially suggested by Dunham et al. (2017). These data indicate higher failure rates for most RAI morphological classes (including intact and discontinuous rock).

Table 3.4 Current and suggested modified RAI activity rates for each morphological classification. Modified from Markus (2018).

RAI class	RAI activity rate		Assumed depth (m)	
	Dunham et al. (2017)	Markus (2018)	Dunham et al. (2017)	Markus (2018)
Unclassified	0.000125	0.0326	0.025	0.1452
Talus	0.000125	0.129	0.025	0.1240
Intact	0.000125	0.0234	0.05	0.1704
10-cm discontinuity	0.002030	0.0306	0.10	0.1724
20-cm discontinuity	0.004600	0.0334	0.20	0.1702
30-cm discontinuity	0.009980	0.0295	0.30	0.2169
Shallow overhang	0.029410	0.0228	0.50	0.2125
Steep overhang	0.039210	0.0362	0.75	0.2316

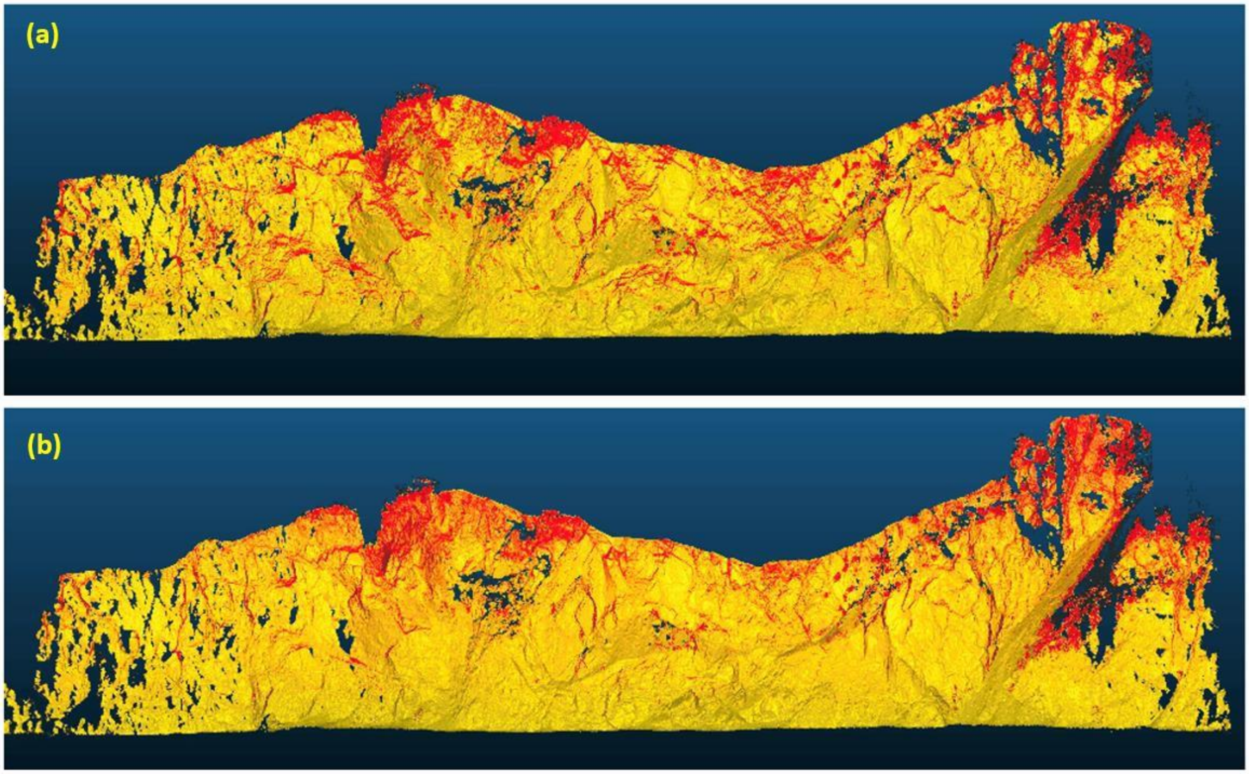

Figure 3.5 Hotspot mapping (a) based on the original RAI activity rates of Dunham et al. (2017) and (b) compared with those derived using the modified RAI activity rates of Markus (2018).

3.2. Mobility Analysis

We computed rockfall volumes for several sites to perform an analysis of mobility impacts using Equation 2 (see Section 1.2) to determine the potential closure times associated with these sites on an annual basis (Table 3.5). The Hewett Lake, Washington (SR 14) site was not used in this analysis because it had been recently scaled, resulting in a substantial amount of additional removed material. Note that this mobility analysis likely overestimated closure time, as not all debris would make it near or onto the highway and require a cleanup. Additionally, the RIM database was developed on the basis of larger, individual failure events rather than a series of smaller events across the rock slope. Nevertheless, at precarious sites there are still partial closures or slowdowns associated with maintenance activities to clean up catch ditches throughout the year or to clean up rocks that have entered the highway. Despite these limitations in using the closure times as absolute values, they still serve as a relative index to prioritize sites for mitigation efforts.

Table 3.5 Rockfall volumes and associated closure times at several rock slope sites.

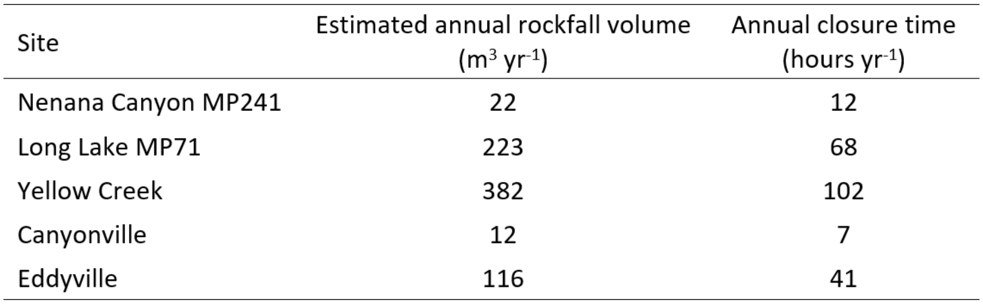

Site	Estimated annual rockfall volume (m^3 yr^{-1})	Annual closure time (hours yr^{-1})
Nenana Canyon MP241	22	12
Long Lake MP71	223	68
Yellow Creek	382	102
Canyonville	12	7
Eddyville	116	41

3.3. Hewett Lake, Washington (SR14) Mitigation Analysis

The Hewett Lake site (SR 14 near MP 73) is located across the Columbia River from the Rowena site studied by Olsen et al. (2020) with similar geology. We completed two surveys of the site; the first was on February 11, 2022, days before scaling operations started, and the second was on August 15, 2022. While there was some erosion signal present in the data, the bulk of the change was due to scaling operations, which removed approximately 2,800 m^3 and affected 5,600 m^2 (21 percent) of the slope (Table 3.6, Figure 3.6).

Table 3.6 Preliminary RAI and change analysis results from the Rambo Software for Hewett Lake site, SR 14 (MP 73).

RAI Class ID	RAI Class Description	Area (m^2)		Percentage (%)		RAI Score (kJ)	
		Before (2/22)	After (8/15)	Before (2/22)	After (8/15)	Before (2/22)	After (8/15)
0	Unclassified	697.1	458.9	1.6	1.0	26,213	18,139
1	Talus	1,619.8	3,358.1	3.7	7.0	10,170	24,270
2	Intact	8,641.7	12,559.7	19.7	26.2	17,969	26,802
3	Fragmented Discontinuous	4,345.8	5,064.8	9.9	10.5	8,835	11,225
4	Closely-spaced Discontinuous	7,945.0	8,268.8	18.1	17.2	24,379	28,698
5	Widely-spaced Discontinuous	9,843.9	8,104.8	22.4	16.9	51,036	45,207
6	Shallow Overhang	10497	9,953.1	23.9	20.7	28,405	25,843
7	Cantilevered Overhang	295.7	241.6	0.7	0.5	564	423
8	Overall	43,886.1	48,009.7	100.0	100.0	167,571	180,606

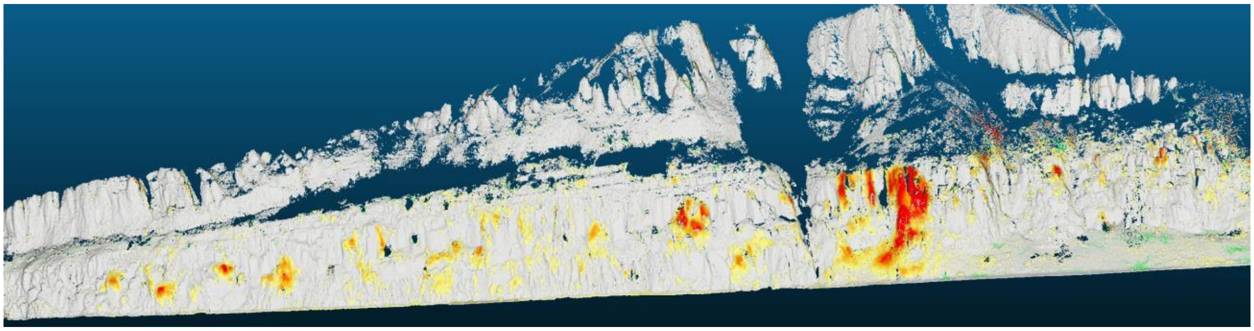

Figure 3.6 Change detection analysis of the Hewett Lake site illustrating locations that were modified during the scaling operations (red colors indicate ≥ 2 m change).

At this site, we observed notable changes, including 1) a decrease in the amount of overhang in the RAI classification (Figure 3.7) and 2) a decrease in the surface roughness (Figure 3.8). Additionally, we observed a substantial increase in the scaling coefficient of the magnitude frequency curves in conjunction with larger block sizes in comparison to the Oregon sites analyzed in Olsen et al. (2020) (Figure 3.9).

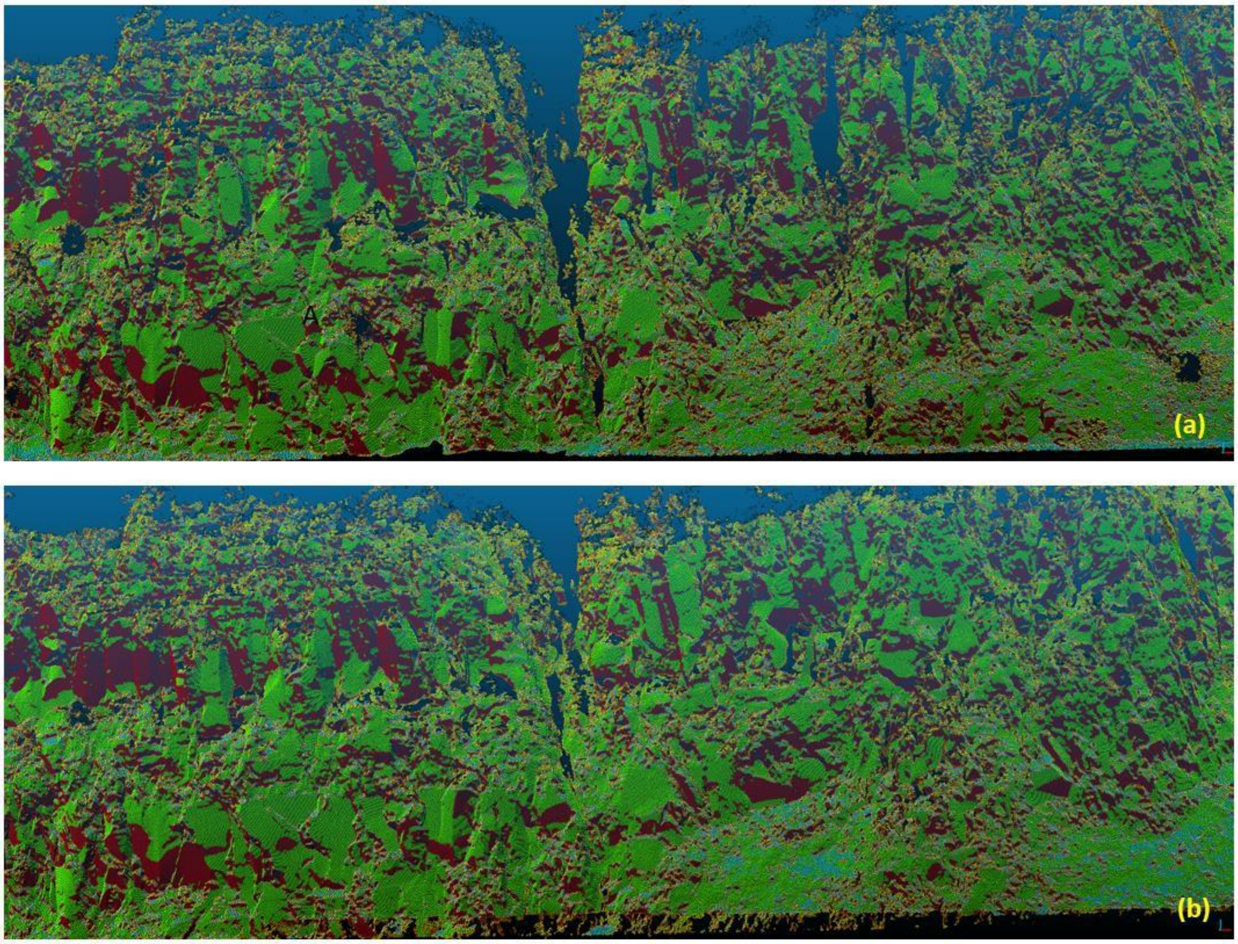

Figure 3.7 Changes in the RAI classification at the Hewett Lake site (a) before and (b) after scaling. Note the reduction in overhang material (red) at several locations along the slope.

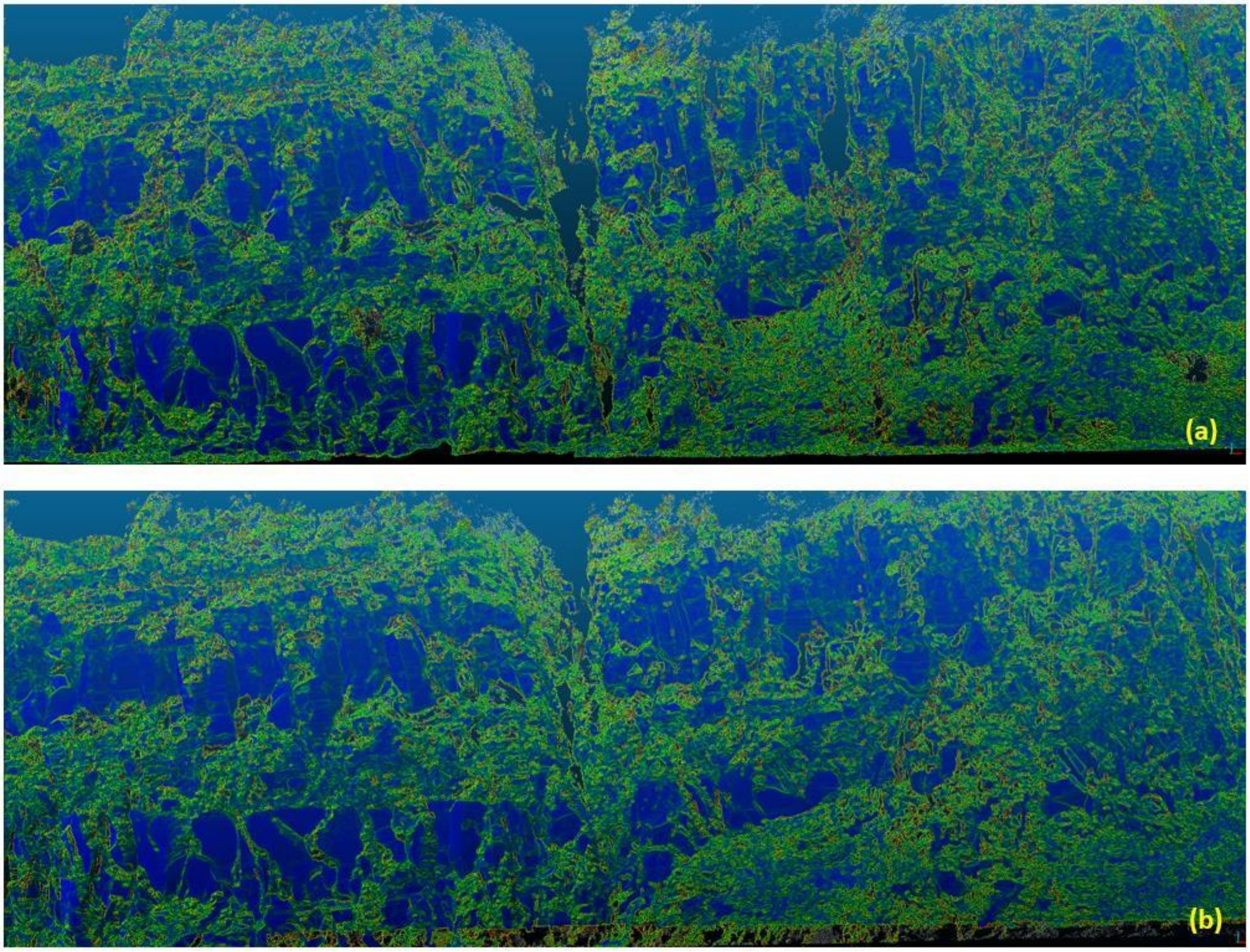

Figure 3.8 Changes in the surface roughness (red, green, and blue indicate high, intermediate, and low roughness, respectively) at the Hewett Lake site (a) before and (b) after scaling. Note low roughness (blue) at several locations along the slope.

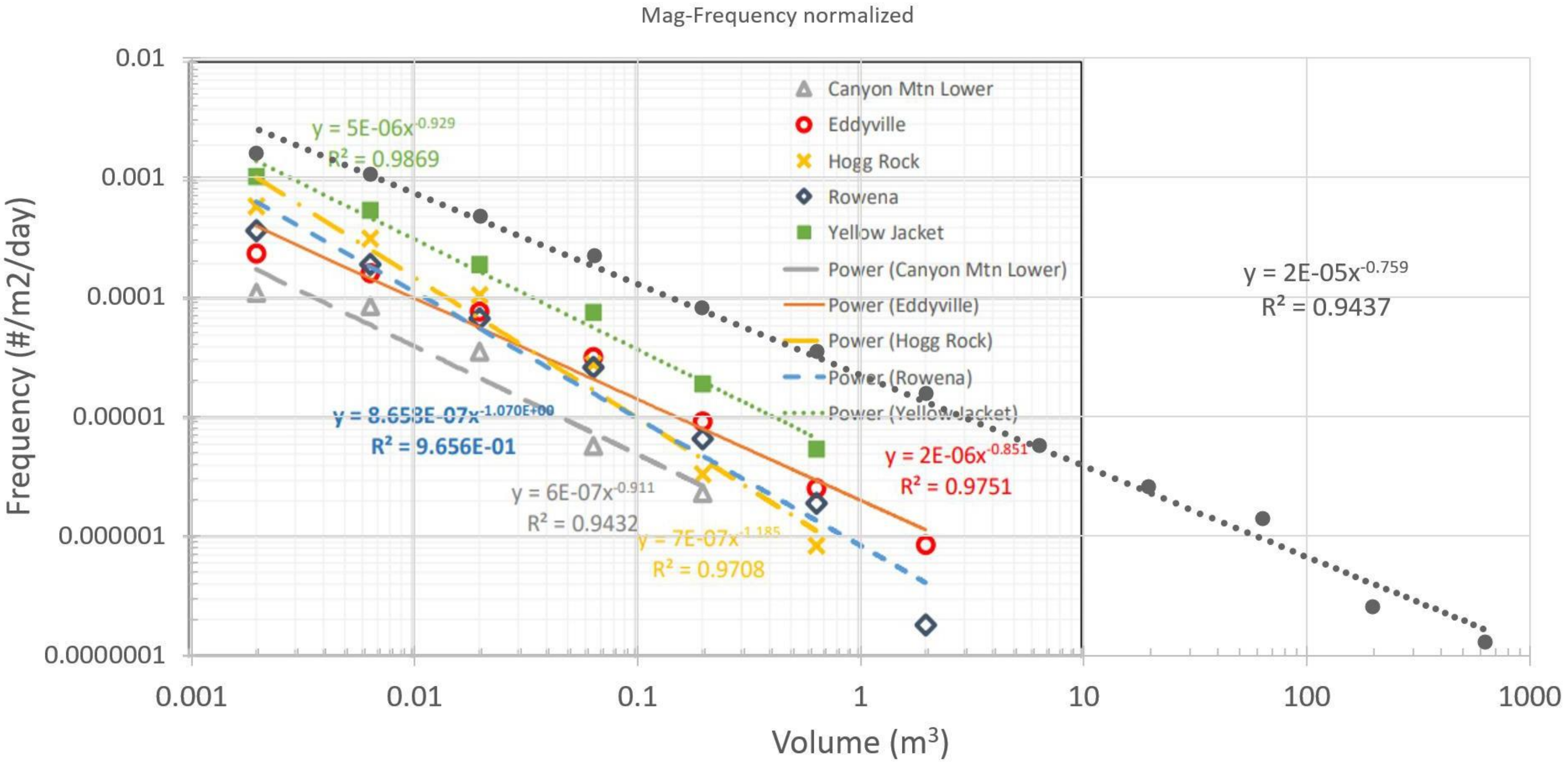

Figure 3.9 Magnitude frequency for the Hewett Lake site during scaling operations (gray dashed line) overlaid on the magnitude frequency curves obtained for the sites in Olsen et al. (2020).

CHAPTER 4. CONCLUSIONS AND OUTREACH

With the support of previous PacTrans funding, members of our research team developed the Rockfall Activity Index system (RAI), a point cloud-derived, high-resolution, morphology-based approach for identifying, assessing, and mapping rockfall hazards at a high resolution across the entire surface of the slope. Ongoing assessment of the RAI indicated that the activity rates are not always consistent, generic values but instead vary as a function of geology and rock material properties. In this project, we continued from and expanded on years of previous PacTrans research by 1) collecting another epoch of terrestrial laser scanning data from six Alaskan sites and four sites in Washington and Oregon, all with extensive rock slopes adjacent to major highways; 2) characterizing the geology and major discontinuities of the Washington and Oregon sites; and 3) collecting 4,800 Schmidt hammer measurements from the field sites for a systematic evaluation of this tool to determine rock strength and to compare rebound values to rockfall activity rates. Coupled with the site characterizations for the Alaska field sites presented by Darrow et al. (2022), the descriptions and discontinuity measurements presented here for the Washington and Oregon sites provide a framework for future studies of these rock slopes, such as kinematic or overall slope stability analyses.

A companion PacTrans-funded project report provides more detail on the Schmidt hammer testing (Herrman and Darrow, in review); however, the systematic comparison of Schmidt hammer measurements to rockfall activity rates presented here demonstrates a modest negative correlation using a power-law relationship. Specifically, there was a tendency to have lower Schmidt hammer rebound values in areas where we observed higher rockfall activity rates. There was, however, variability in these results, and we suggest that such analyses should be evaluated on a site-by-site basis. An evaluation of uncorrected and corrected (per ASTM standards) Schmidt hammer rebound values demonstrated that the correction procedure provides a modest improvement of the correlation with rockfall activity.

Further research could explore whether other correction procedures provide better, more representative fits, including that associated with user bias.

Activity rates at each site varied significantly by year, but median and average values demonstrated reasonable correlation with the Schmidt hammer rebound values. We suggest that prolonged monitoring and lidar differencing, as well as repeated collection of Schmidt hammer measurements, may lead to reduced uncertainty and more robust correlations, potentially at scales more generalizable to other rock slopes. Evaluation of more geologic units with diverse structural controls may demonstrate the utility (or lack thereof) of Schmidt hammer measurements as a proxy for rockfall activity rates. Furthermore, we recommend using the activity values suggested by Markus (2018) as the baseline parameters for RAI analysis; and if SH data are available and less than 20, we recommend adopting the upper range of failure rate values presented in this report.

On the basis of our analyses, we identified the following areas of future research:

- While the approaches that we used accurately quantify that material has fallen from the rock slope, the amount of material that enters the roadway and has direct mobility impacts is not well understood. Additionally, we did not investigate the impact on maintenance activities to clean debris from the catch ditches. Anecdotal accounts from conversations with maintenance personnel indicate that they frequently observe small rock debris entering the road that requires cleaning. Ultimately, a scale factor would help to calibrate the application of the RIM model to produce more realistic closure time values based on material that requires immediate cleanup. Because the RIM model was developed on the basis of larger episodic events, an additional model based on smaller, more frequent events would be useful to quantify shorter but more frequent delays to motorists.
- The long-term effectiveness of rock slope modification techniques and the associated impacts on mobility have not been quantified. While this research and previous PacTrans research indicated a reduction in RAI scores by reducing the amount of overhang, the long-term evolution of the rock slopes requires further investigation. Future research can evaluate the impacts of these modifications to reduce the estimates of material entering the highway.

4.1. Outreach\Technology Transfer

For outreach and technology transfer of this research and research from previous PacTrans projects, the research team organized and delivered a webinar through the National Academies of Science, Engineering, and Technology, Committee on Geological and Geotechnical Engineering (COGGE). The webinar was entitled “Effective Utilization of State-of-the-Art Geospatial Technology for Geotechnical Investigations and Monitoring: The Future is Now.” Panelists came from industry, government, and academic backgrounds with diverse experience in geotechnical applications, including Drs. Michael Olsen, Ben Leshchinsky, Chris Massey (GNS), and Zhangwei Ning (Sixense). This webinar explored examples of how geospatial technologies are used effectively in practice, the capabilities and limitations of the technology, and considerations for selecting which technologies are most suitable for a project. Work from this and prior PacTrans projects for slope monitoring were included. Over 500 people attended the webinar. A recording of the webinar is available at https://www.youtube.com/watch?v=s7vfaCdn_fM.

Members of the research team held a trial all-day RAI training workshop hosted by ODOT in late 2021. Owing to restrictions for in-person meetings because of the COVID-19 pandemic, the event was held in a virtual format. Approximately 20 staff members from ODOT attended the interactive event.

Presentation and activity topics included a review of the fundamental aspects of the RAI system and its associated input parameters, a discussion of RAI computer modeling and integration with software programs, and interpretation of RAI results and output, including identification and mapping of hotspots of rock slope activity. The ODOT training exercise served as a trial for an anticipated series of in-person training modules developed by the project research team. These modules will be targeted to the staff of departments of transportation, practicing engineers and geoscientists, and students in civil engineering and engineering geology. Potential venues for future training events include the annual Transportation Research Board meeting in Washington, D.C. and conferences such as the American Society of Civil Engineers Geo-Institute and the annual meeting of the Association of Environmental and Engineering Geologists. The workshop presentation materials are available upon request from the project team and will be continuously updated as additional training events occur.

REFERENCES

Alaska Department of Transportation and Public Facilities (ADOT&PF), 2020. Alaska DOT&PF Route Centerlines. Fairbanks, Alaska Department of Transportation and Public Facilities. Available from: < https://dot.alaska.gov/stwddes/gis/shapefiles.shtml>

Alaska Geospatial Council (AGC), 2020. Alaska Coastline Shapefiles. Fairbanks, Alaska Geospatial Office. Available from: < https://gis.data.alaska.gov/search?q=alaska%20boundary >

ASTM International, 2014. *Standard Test Method for Determination of Rock Hardness by Rebound Hammer Method, D5873-14:* ASTM International, West Conshohocken, PA, 6 p.

Attewell, P.B., and Farmer, I W. (1976). *Principles of Engineering Geology*: Chapman and Hall, London. Aydin, A. and Basu, A., 2005. "The Schmidt hammer in rock material characterization." *Engineering Geology*: 81(1), 1-14, https://doi.org/10.1016/j.enggeo.2005.06.006

Aydin, Adnan & Basu, Arindam. (2005). The Schmidt Hammer in rock material characterization. Engineering Geology. 81. 1-14. 10.1016/j.enggeo.2005.06.006.

Darrow, M. M., Herrman, D. M., Holtan, K, Leshchinsky, B., Olsen, M., Wartman, J., 2022. *The Long-Term Effect of Earthquakes: Using Geospatial Solutions to Evaluate Heightened Rockfall Activity on Critical Lifelines*: PacTrans, Seattle, WA, 74 p.

Dunham, L., Wartman, J., Olsen, M. J., O'Banion, M. S., Cunningham, K., 2017. Rockfall Activity Index (RAI): a lidar-derived, morphology-based method for hazard assessment. *Engineering Geology*, 221: 184-192.

Herrman, D. M. and Darrow, M. M., In Review. *Hammer Time: Using the Schmidt Hammer to Improve the Rockfall Activity Index (RAI) Forecasting Accuracy:* PacTrans, Seattle, WA.

Holtan, K., 2021. *Assessing Seismic Rockfall Impacts on Mobility in Transportation Corridors*: MS Thesis, Oregon State University, 105 p.

Johnson, M. G. and Page, N. J., 1979. *Preliminary Geologic Map of the Metavolcanic and Associated Rocks in Parts of the Canyonville, Days Creek, and Glendale Quadrangles, Oregon*: Open-File Report 79-283, US Geological Survey, 1:62,500.

Korosec, M. A., 1987. *Geologic Map of the Hood River Quadrangle, Washington and Oregon*: Washington Division of Geology and Earth Resources Open File Report 87-6, Washington State Department of Natural Resources, 46 p.

Markus, S. J., 2018. *Morphological Evolution of Rock-Slopes and Assessing the Rockfall Activity Index (RAI) Methodology*: MS Thesis, University of Washington.

Niem, A. R. and Niem, W. A., 1990. *Geology and Oil, Gas, and Coal Resources, Southern Tyee Basin, Southern Coast Range, Oregon*: Open-File Report O-89-3, State of Oregon Department of Geology and Mineral Resources, 105 p.

Olsen, M. J., Massey, C., Senogles, A., Leshchinsky, B. A., Wartman, J., 2020. *Predicting Seismic-Induced Rockfall Hazard for Targeted Site Mitigation*: Oregon Department of Transportation Research Section and the Federal Highway Administration, SPR-809, 378 p.

Oregon Geospatial Enterprise Office (OGEO), 2023a. Oregon Highway Network. Oregon Geospatial Enterprise Office. Available from: <

Oregon Geospatial Enterprise Office (OGEO), 2023b. Oregon Area Commissions on Transportation - 2010. Oregon Geospatial Enterprise Office. Available from:< https://www.oregon.gov/geo/pages/sdlibrary.aspx >

Snavely, P. D., MacLeod, N. S., Wagner, H. C., Rau, W. W., 1976. *Geologic Map of the Yaquina and Toledo Quadrangles, Lincoln County, Oregon*: Miscellaneous Investigations Series Map I-867, US Geological Survey, 1:62,500.

Wang, M. and Wan, W., 2019. "A new empirical formula for evaluating uniaxial compressive strength using the Schmidt hammer test." *International Journal of Rock Mechanics and Mining Sciences*: 123, 104094, https://doi.org/10.1016/j.ijrmms.2019.104094

Washington State Department of Natural Resources (WA DNR), 2023a. WA_State_Boundary. Washington State Department of Transportation Geospatial Open Data Portal. Available from: < https://data-wadnr.opendata.arcgis.com/search?groupIds=eee2501342024deaaa41a61c48321d42 >

Washington State Department of Natural Resources (WA DNR), 2023b. WSDOT – State Route Line (1:24K) 2012. Washington State Department of Transportation Geospatial Open Data Portal. Available from: < https://gisdata-wsdot.opendata.arcgis.com/ >